Cerebral Cortex, October 2015;25: 3911–3931

doi: 10.1093/cercor/bhu277
Advance Access Publication Date: 1 December 2014
Original Article

ORIGINAL ARTICLE

Probabilistic Maps of Visual Topography in Human Cortex

Liang Wang[1,2,3,†], Ryan E.B. Mruczek[1,2,4,†], Michael J. Arcaro[1,2], and Sabine Kastner[1,2]

[1]Princeton Neuroscience Institute and, [2]Department of Psychology, Princeton University, Princeton, NJ 08544, USA, [3]Key Laboratory of Mental Health, Institute of Psychology, Chinese Academy of Sciences, Beijing 100101, China, and [4]Department of Psychology, Swarthmore College, Swarthmore, PA 19081, USA

Address correspondence to Liang Wang, Key Laboratory of Mental Health, Institute of Psychology, Chinese Academy of Sciences, 16 Lincui Rd., Chaoyang District, Beijing 100101, China. Email: lwang@psych.ac.cn; Sabine Kastner, Department of Psychology, Princeton Neuroscience Institute, Washington Road, Princeton, NJ 08544, USA. Email: skastner@princeton.edu

[†]These authors contributed equally to this work.

Abstract

The human visual system contains an array of topographically organized regions. Identifying these regions in individual subjects is a powerful approach to group-level statistical analysis, but this is not always feasible. We addressed this limitation by generating probabilistic maps of visual topographic areas in 2 standardized spaces suitable for use with adult human brains. Using standard fMRI paradigms, we identified 25 topographic maps in a large population of individual subjects ($N = 53$) and transformed them into either a surface- or volume-based standardized space. Here, we provide a quantitative characterization of the inter-subject variability within and across visual regions, including the likelihood that a given point would be classified as a part of any region (full probability map) and the most probable region for any given point (maximum probability map). By evaluating the topographic organization across the whole of visual cortex, we provide new information about the organization of individual visual field maps and large-scale biases in visual field coverage. Finally, we validate each atlas for use with independent subjects. Overall, the probabilistic atlases quantify the variability of topographic representations in human cortex and provide a useful reference for comparing data across studies that can be transformed into these standard spaces.

Key words: atlas, cortical organization, functional magnetic resonance imaging, mapping, topography

Introduction

Primate cortex has been subdivided into a multitude of areas based on anatomy and function. Cortical regions have been delineated based on their cytoarchitecture (Schleicher et al. 2005), neurotransmitter receptor distributions (Zilles and Amunts 2009), genetic markers (Chen et al. 2012), patterns of anatomical connections (Passingham et al. 2002), and their functional response properties (Op de Beeck et al. 2008). With regard to functional organization, the primate visual system represents one of the most thoroughly studied cortical systems. Evidence from monkey neurophysiology and human neuroimaging has identified a series of discrete cortical regions implicated in the analysis of visual information (Felleman and Van Essen 1991; Wandell and Winawer 2011). Individual regions can be delineated based on the representation of spatial information in the form of discrete retinotopic maps, with each visual area containing a quarter- or half-field representation of contralateral visual space. Based on these criteria, over 25 topographic regions in occipital, ventral–temporal, parietal, and frontal cortex have been identified in the human brain (Silver and Kastner 2009; Wandell and Winawer 2011).

One standard approach to studying the human visual system is to "map" each of these areas in individual subjects and to subsequently explore the response properties of each area in

independent experiments. This "region-of-interest" (ROI) approach is a powerful way to combine data across subjects (Saxe et al. 2006), under the assumption that each ROI represents a meaningful and consistent division of cortex. Current neurophysiology and neuroimaging techniques provide sufficient spatial resolution to dissociate the responses of individual areas and both have utilized the ROI approach to characterize the response properties of different portions of the primate visual system.

Despite its strengths, the retinotopic mapping approach has significant practical limitations. First, although current fMRI scanners have sufficient spatial resolution to identify different visuotopic regions, it is a time consuming and expensive process. For example, although all retinotopically defined regions reflect a similar underlying spatial organization, different regions may be best-identified using different stimuli and experiential parameters. Early visual areas are typically mapped with passively viewed "wedge and ring" stimuli (Sereno et al. 1995; DeYoe et al. 1996; Engel et al. 1997) with relatively short stimulus cycles of 24 or 32 s (the length between stimulus position repetitions) and relatively thick wedges (90°), and can be identified in a short scan session. Higher order regions with larger receptive fields, such as TO1/2, VO1/2, and PHC1/2, are better identified using a longer stimulus cycle (40 or 64 s), thinner wedges (45°), and typically require a longer scan session (Wandell et al. 2007; Kolster et al. 2010). Topographic regions of the parietal and frontal cortices are often identified using a completely different memory-guided saccade mapping procedure (Sereno et al. 2001), which incorporates covert attention, spatial memory, and overt saccades in a traveling-wave paradigm. Finally, many visual areas appear to benefit from combining aspects of the two methods by employing a concurrent covert attention-monitoring task with a traditional wedge stimulus (Arcaro et al. 2009; Bressler and Silver 2010). In total, identifying all of the currently known topographic regions of the human visual system requires multiple scanning sessions. Given the expense and availability of fMRI, this is not always practical.

A second limitation of the retinotopic mapping approach is comparing results from studies using other methods that are not easily integrated with fMRI. For example, electrocorticography (ECoG) in pre-surgical epilepsy patients and the anatomical and functional analysis of patients with neurological disorders or traumatic brain injury provide rich datasets with which to study the human brain. Anatomical brain scans of these patients may allow for a transformation of electrode coordinates or lesion sites into standard space (e.g., Talairach or MNI space), but it is often not feasible to obtain detailed retinotopic mapping of the patient's brain (but see, e.g., Konen et al. 2011; Parvizi et al. 2012). Thus, there are practical limitations to relating results from studies using these methods to retinotopically defined cortical organization.

One way to address these limitations is to create an atlas in a standard space that links individual points in that space with functionally defined regions. Given the anatomical and functional variability across subjects, this atlas should be "probabilistic," in that it defines the likelihood of a given coordinate being associated with a given functional region. Such an atlas could be used to infer the topographic location in the visual system for the results obtained from any independent dataset once transformed into the same standard space as the atlas. This approach has recently been advanced for cortical parcellation schemes based on the quantitative analysis of cytoarchitecture in post-mortem human brains (Schleicher et al. 2005).

In the current study, we describe 2 such probabilistic atlases of 25 topographically defined regions, covering 22 areas of the human visual system. Each region was defined in individual subjects and transformed into one of the two standard spaces: a cortical surface alignment to a standard surface space (Buckner40 template in Freesurfer; Fischl, Sereno, Tootell et al. 1999) or a nonlinear volume normalization to MNI space (Collins et al. 1994; Andersson et al. 2007). We carried out a constellation of analyses to quantify the characteristics of the atlases and validate them with respect to the areas defined in individual subjects. Compared with the volume-based atlas, the surface-based atlas was relatively better at preserving the spatially topologic structure across the visual system and aligning to topographic areas defined in novel subjects. Moreover, the atlas was also successful at predicting the pattern of functional connectivity across all visual regions from resting-state data. These atlases will be made freely available in formats that are compatible with several major fMRI analysis packages (e.g., FSL, AFNI, and SUMA; see www.princeton.edu/~napl/vtpm.htm).

Materials and Methods

Subjects

Fifty-three human subjects (31 males) gave informed written consent for participation in this study. All subjects except for one reported that they were right-handed (one left-handed), had normal or corrected-to-normal vision, and were in good health with no history of neurological disorders. All subjects participated in 1 or 2 scan sessions for standard retinotopic mapping and/or memory-guided saccade mapping. Table 1 shows the final number of subjects whose data contributed to every ROI defined in the probabilistic atlas. In total, the current dataset was collected over several years, although multiple scanning sessions for any individual subject occurred within a few months of each other. Twelve subjects additionally participated in a separate scanning session to acquire a task-free (i.e., resting-state) dataset. All procedures were approved by the Institutional Review Board of Princeton University.

Stimulus Presentation

Stimuli were presented using a Macintosh G4, G5 or Pro computer (Apple Computers, Cupertino, CA, USA) running MATLAB (The MathWorks, Natick, MA, USA) and the Psychophysics Toolbox (Version 3, Brainard 1997; Pelli 1997), or Vision Egg software (Straw 2008). Visual stimuli were projected from a Powerlite 7250 liquid crystal display projector (Epson, Long Beach, CA, USA; Allegra setup) or a Hyperion MRI Digital Projection System (Psychology Software Tools, Sharpsburg, PA, USA; Skyra setup) onto a translucent screen located at the end of the scanner bore, which subjects viewed through a mirror attached to the head coil. The projection covered a circular region of 30° of visual angle (Allegra setup) or a rectangular region of 28 × 48° of visual angle (Skyra setup). In all experiments, stimulus presentation was time-locked to fMRI acquisition via a trigger from the scanner at the start of image acquisition.

Experimental Tasks

Retinotopic Mapping

Standard retinotopic mapping was performed for each subject using a color and luminance varying flickering checkerboard stimulus (Swisher et al. 2007; Arcaro et al. 2009). The detailed description of the design is given elsewhere (Arcaro et al. 2009). Briefly, subjects performed 3–5 runs of polar angle mapping and 2 runs of eccentricity mapping, each comprised eight 32 s

Table 1 Number of subjects contributing to the probabilistic atlas for each ROI and reference(s) for their border definitions, as used for the atlas

ROI	Subjects (N_{LH},N_{RH})	Reference
Ventral–temporal		
V1v	50, 50	Sereno et al. (1995), DeYoe et al. (1996) and Engel et al. (1997)
V2v	50, 50	Sereno et al. (1995), DeYoe et al. (1996) and Engel et al. (1997)
V3v	50, 50	Sereno et al. (1995), DeYoe et al. (1996) and Engel et al. (1997)
hV4	50, 50	Wade et al. (2002)
VO1	50, 50	Brewer et al. (2005)
VO2	49, 49	Brewer et al. (2005)
PHC1	47, 47	Arcaro et al. (2009)
PHC2	43, 46	Arcaro et al. (2009)
Dorso-lateral		
V1d	50, 50	Sereno et al. (1995), DeYoe et al. (1996) and Engel et al. (1997)
V2d	50, 50	Sereno et al. (1995), DeYoe et al. (1996), Engel et al. (1997)
V3d	50, 50	Sereno et al. (1995), DeYoe et al. (1996) and Engel et al. (1997)
V3A	50, 50	Press et al. (2001)
V3B	50, 50	Press et al. (2001)
LO1	50, 50	Larsson and Heeger (2006)
LO2	50, 50	Larsson and Heeger (2006)
TO1	48, 43	Amano et al. (2009)
TO2	48, 44	Amano et al. (2009)
Parietal and Frontal		
IPS0	31, 31	Konen and Kastner (2008)
IPS1	32, 32	Konen and Kastner (2008)
IPS2	32, 32	Konen and Kastner (2008)
IPS3	32, 32	Konen and Kastner (2008)
IPS4	32, 32	Konen and Kastner (2008)
IPS5	32, 32	Konen and Kastner (2008)
SPL1	32, 32	Konen and Kastner (2008)
hFEF	32, 32	Kastner et al. (2007)

or 40 s stimulus cycles. Subjects maintained central fixation and performed a dimming detection task either at central fixation or embedded within the checkerboard stimulus. Polar angle and eccentricity representations were extracted from separate runs using standard phase encoding techniques (Bandettini et al. 1993; Sereno et al. 1995; Engel et al. 1997).

Memory-Guided Saccade Mapping

Memory-guided saccade mapping was used to localize topographically organized areas in parietal and frontal cortex (Kastner et al. 2007; Konen and Kastner 2008). This task incorporates covert shifts of attention, spatial working memory, and saccadic eye movements in a traveling-wave paradigm. The detailed description of the design is provided elsewhere (Kastner et al. 2007; Konen and Kastner 2008). Briefly, subjects had to remember and attend to the location of a peripheral cue over a delay period while maintaining central fixation. After the delay period, the subject had to execute a saccade to the remembered location and then immediately back to central fixation. The target cue was systematically moved on subsequent trials either clockwise or counterclockwise among 8 equally spaced locations. Subjects performed 8 runs, each composed of eight 40 s cycles of the sequence of 8 target positions. Fourier analysis (Bandettini et al. 1993; Engel et al. 1997; Sereno et al. 2001) was used to identify voxels that were sensitive to the spatial position (i.e., polar angle) of a peripheral cue during the task.

Resting State

Twelve subjects also participated in 2 versions of resting state: (1) fixation and (2) eyes closed. During the fixation scans, subjects were instructed to maintain fixation on a centrally presented dot (0.3° diameter) overlaid on a mean grey luminance screen background for 10 min. During the eyes closed scans, the projector was turned off and subjects were instructed to keep their eyes closed for 10 min. Two runs were collected per resting condition and data from all 4 runs were used for the analysis of the resting-state data.

Data Acquisition

Data were acquired with a Siemens 3T Allegra scanner using a standard head coil or a Siemens 3T Skyra scanner using a 16-channel phased-array head coil (Siemens, Erlangen, Germany). Functional images were acquired with a gradient echo, echo planar sequence using an interleaved acquisition. The specific parameters for each scan session are outlined below.

Retinotopic Mapping

Twenty-five coronal (Allegra) or 31 axial (Skyra) slices covering occipital, posterior–parietal, and temporal cortex were acquired (128 × 128 matrix, 256 × 256 mm field of view [FOV], 2 × 2 mm in-plane resolution, 2 mm slice thickness with 1 mm gap or 3 mm slice thickness, 2.5 s repetition time [TR], 40 ms echo time [TE], 75 or 90° flip angle [FA]). Scanning at the Allegra used a partial Fourier factor of 7/8 to sample an asymmetric fraction of *k*-space and reduce acquisition time. Scanning at the Skyra used a generalized auto-calibrating partially parallel acquisition (GRAPPA) sequence with an acceleration factor of 2.

In addition, an in-plane magnetic field map image (2 × 2 mm in-plane resolution, 2 mm slice thickness, same gap as functional scans, 0.5 s TR, 5.23 or 7.69 ms TE, 55° FA) was acquired to perform echo planar image undistortion (Jezzard and Balaban 1995; Jenkinson 2001). In each session, a high-resolution anatomical scan (magnetization-prepared rapid-acquisition gradient echo sequence, MPRAGE; Allegra: 256 × 256 matrix; 256 × 256 mm FOV; 1 mm isotropic resolution; 2.5 s TR, 4.38 ms TE; 8° FA; Skyra: 256 × 256 matrix; 240 × 240 mm FOV; 0.9375 × 0.9375 mm in-plane resolution; 0.9 mm slice thickness; 1.9 s TR, 2.13 ms TE; 9° FA; GRAPPA acceleration factor of 2) was acquired to facilitate alignment of functional data with the cortical surface.

Memory-Guided Saccade Mapping

The scanning parameters (including field map and structural scan) were the same as for the retinotopic mapping, except we acquired axial slices covering parietal, frontal, and dorsal occipital cortex.

Surface Reconstruction

For each subject, 2 high-resolution structural scans (MPRAGE, same parameters as above) were acquired in one of the scanning sessions, averaged, and used for cortical surface reconstruction.

Resting State

Thirty-two slices covering the whole-brain were acquired at the Skyra (64 × 64 matrix, 192 × 192 mm FOV, 3 × 3 mm in-plane resolution, 3 mm slice thickness, 1.8 s TR, 30 ms TE, 72° FA). A high-resolution structural scan was acquired for registration

to surface anatomical images (MPRAGE, same parameters as above).

Data Analysis

Imaging data were analyzed using AFNI (http://afni.nimh.nih.gov/afni/) (Cox 1996), SUMA (http://afni.nimh.nih.gov/afni/suma) (Saad et al. 2004), FSL (http://www.fmrib.ox.ac.uk/fsl/) (Smith et al. 2004; Woolrich et al. 2009), FreeSurfer (http://surfer.nmr.mgh.harvard.edu/) (Dale et al. 1999; Fischl, Sereno and Dale 1999) and MATLAB.

Data Preprocessing

Details of the data analysis for the retinotopic and memory-guided saccade mapping are provided elsewhere (Kastner et al. 2007; Konen and Kastner 2008; Arcaro et al. 2009). Briefly, functional images were slice-time and motion corrected, field map undistorted, and smoothed with a 2–4 mm full-width half-max Gaussian kernel. The in-session anatomical volume was aligned to the unsmoothed functional images to account for subject movement between functional and anatomical acquisition, and subsequently the high-resolution anatomical volume used for surface reconstruction was aligned with the in-session anatomical volume. Both alignments were performed with a 6-parameter rigid-body transformation without warping or shearing. Since they were limited to the anatomical volumes, the functional data were not interpolated at this stage. After alignment, the smoothed functional volume data were projected to the cortical surface. Finally, Fourier analysis was used to identify the phase (i.e., polar angle or eccentricity) at which the stimulus frequency was represented in the functional time course.

Resting-state fMRI data were slice-time and motion corrected. In preparation for functional connectivity analyses, several additional steps were performed including (1) removal of potential "spike" artifacts using AFNI's 3dDespike, (2) temporal filtering retaining frequencies in the 0.01–0.1 Hz band, and (3) linear and quadratic detrending. To minimize the effect of any evoked response due to the scanner onset, the initial 20 s (i.e., 11 volumes) were removed. The average time-series from each of the visual areas described below was extracted into MATLAB for correlation analyses.

Regions of Interest

The averaged high-resolution structural images were used to reconstruct a cortical surface model for each subject using Freesurfer. Polar and eccentricity angle phase maps were projected onto each subject's reconstructed surface and borders between different ROIs were delineated by reversals in polar angle representation at or near the horizontal meridian (HM), upper vertical meridian (UVM), and/or lower vertical meridian (LVM). Although there have been some approaches to identifying borders of some topographic areas using automated algorithms, particularly in early visual cortex (e.g., Dumoulin et al. 2003; Larsson and Heeger 2006), these algorithms either fail or have not been tested for many higher-order regions. Thus, we used the conventional approach of drawing are borders by hand. In all cases, at least 2 experimenters experienced in retinotopic mapping drew borders independently using the same set of published criteria (detailed below) and subsequently resolved any inconsistencies. The correspondence between the atlas borders (derived from the hand-drawn maps, see below) and the group-averaged phase maps (derived directly from the phase data itself, see below) indicates that the criteria for defining borders was applied consistently across subjects (see Fig. 4 and Supplementary Fig. 4).

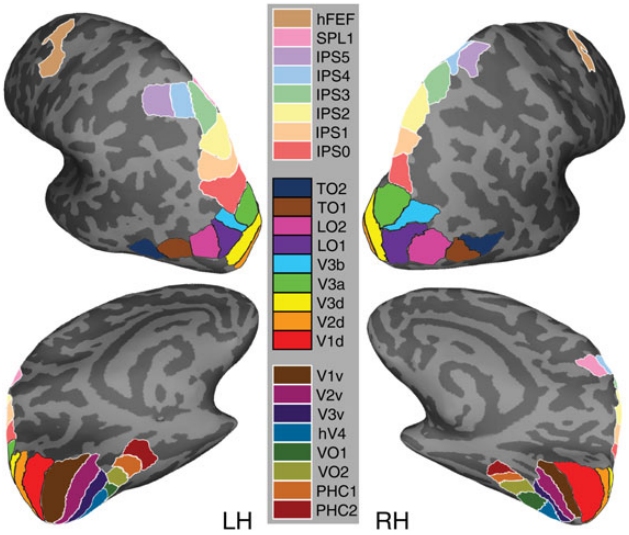

Figure 1. Schematic borders of 25 topographic visual regions from a representative subject. The areas outlined on the inflated cortical surface were delineated in individual subjects and used to generate the surface-based atlas. Note that ventral (upper visual field) and dorsal (lower visual field) representations for early visual cortex areas V1–V3 were defined separately. Note also that the grouping of ROIs into ventral–temporal (lower legend), dorsal–lateral (middle legend), and parietal–frontal (upper legend) is only for the purpose of organizing the presentation of the data and should not be taken to indicate distinct information processing hierarchies of the visual system. Example polar angle maps from individual subjects are presented in Supplementary Figures 1–3.

We note, however, that a more objective method of marking visual area borders remains a worthy goal and would potentially increase the precision for the group-averaged data.

In total, 25 topographic surface areas in each hemisphere were defined (details below), comprising 8 ventral–temporal (V1v, V2v, V3v, hV4, VO1, VO2, PHC1, and PCH2), 9 dorsal–lateral (V1d, V2d, V3d, V3A, V3B, LO1, LO2, TO1, and TO2), 7 parietal (IPS0, IPS1, IPS2, IPS3, IPS4, IPS5, and SPL1), and one frontal (hFEF) regions (for review including functional response properties, see Silver and Kastner 2009; Wandell and Winawer 2011). Note that ventral (upper visual field) and dorsal (lower visual field) representations for visual areas V1, V2, and V3 were defined separately. Thus, the current dataset covers 25 topographic maps comprising 22 visual regions of human cortex. We use the term ROI to indicate one of the 25 distinct topographic regions included in our analysis. It should be noted that the grouping of ROIs as ventral–temporal, dorsal–lateral, etc. in this section and the results is done for the purpose of organizing the presentation of the data and should not be taken to indicate distinct information processing hierarchies of the visual system.

Figure 1 shows the borders of the 25 ROIs for one example subject. Table 1 shows the total number of subjects that contributed data for each ROI, along with references that were used for ROI border definitions. In this study, we refer to ROIs defined in an individual subject (i.e., in that subject's native space) as "subject-specific" ROIs.

Posterior–Occipital ROIs. Six topographic areas (V1v and V1d; V2v and V2d; and V3v and V3d) were defined in occipital visual cortex (Sereno et al. 1995; DeYoe et al. 1996; Engel et al. 1997). For our atlas, the ventral and dorsal portions of visual areas V1, V2, and V3 were defined separately. Thus, each region contained a quarter-field representation of the upper (ventral ROIs) or lower (dorsal ROIs) contralateral visual field.

For the ventral–occipital regions, V1v extended from an HM in the fundus of the calcarine sulcus to an UVM forming the border of V1v and V2v. V2v extended from this UVM to an HM forming the border of V2v and V3v. The ventral-anterior border of V3v was formed by a representation of the UVM at the border of hV4 and VO1. For the dorsal–occipital regions, V1d extended from an HM in the fundus of the calcarine sulcus to a LVM forming the border of V1d and V2d. V2d extended from this LVM to an HM forming the border of V2d and V3d. The anterior-lateral border of V3d was formed by a representation of the LVM at the border of V3A/B and LO1. All posterior–occipital areas—V1, V2, and V3—shared a foveal confluence, with the peripheral representation extending toward the collateral sulcus.

Ventral–Temporal ROIs. Five topographic regions (hV4, VO1, VO2, PHC1, and PHC2) were defined in ventral–occipital–temporal cortex with their general progression being posterior to anterior. Adjacent and ventral-lateral to the UVM of V3v, hV4 encompassed a representation of contralateral space that extended to a lateral border formed by LVF angles. The fovea of hV4 was continuous with the foveal confluence shared by early visual areas V1–3, with the peripheral representation extended toward the collateral sulcus and parallel with the eccentricity map of ventral V1–3. As observed previously (Hansen et al. 2007; but see Winawer et al. 2010), the anterior border of hV4 was formed by either a continuous representation of the LVM or a discontinuous representation of the LVM intermixed with an HM representation. We defined the anterior-medial aspect of this border as the most peripheral representation that reversed back toward a distinct foveal representation along the posterior–lateral bank of the collateral sulcus. Overall, our definition of hV4 is consistent with the model proposed by Wade et al. (2002), and is distinct from the topography observed in macaque V4, which contains a quarter-field representation (Gattass et al. 1988; Wade et al. 2002; Brewer et al. 2005).

Two cortical areas (VO1 and VO2), each containing a representation of contralateral space, extended anterior to hV4 (Brewer et al. 2005; Arcaro et al. 2009). VO1 shared an LVM representation with hV4. The border between hV4 and VO1 was defined by a reversal in eccentricity representation within the periphery (Brewer et al. 2005; Arcaro et al. 2009; Witthoft et al. 2013). VO1 and VO2 were located along the posterior–medial fusiform gyrus and within the posterior portion of the collateral sulcus and shared an UVM representation along their border. VO2 extended anterior from this UVM to an LVM, forming the border of VO2 and PHC1. Along the posterior part of the medial fusiform gyrus, VO1/2 typically shared a foveal representation that was distinct from the large foveal confluence shared by V1–3 and hV4. The lateral border of VO1, abutting hV4, was identified as the peripheral extent of the eccentricity representation.

Two cortical areas (PHC1 and PHC2), each containing a representation of contralateral space, were identified anterior to VO2 (Arcaro et al. 2009). The posterior border of PHC1 was shared with the anterior border of VO2 at an LVM. PHC1 and PHC2 were located within the posterior parahippocampal cortex, extending along the collateral sulcus and flanked by the lingual gyrus and the posterior portion of the parahippocampal gyrus on one side and the medial fusiform gyrus on the other side. The border between PHC1 and PHC2 was defined by a representation of the UVM. The anterior border of PHC2 was formed by an LVM.

Dorsal–Occipital ROIs. Two cortical areas (V3A and V3B), each containing a representation of contralateral space, were identified near the transverse occipital sulcus (Tootell et al. 1997; Smith et al. 1998; Press et al. 2001). Both V3A and V3B extend from a posterior–medial border with V3 at an LVM to an anterior–dorsal UVM representation. The anterior–dorsal extent of V3A and V3B forms a border with IPS0/V7 (Tootell et al. 1998; Press et al. 2001). V3A and V3B shared a border that divides a shared representation of central space that is separate from the foveal confluence of early visual areas V1–V3.

Lateral–Occipital–Temporal ROIs. Two cortical areas (LO1 and LO2), each containing a representation of contralateral space, were identified in lateral–cortex extending from V3d (Larsson and Heeger 2006). The posterior border of LO1 was shared with the anterior-lateral border of V3d at an LVM. LO1 and LO2 were separated by an UVM representation. LO2 extended anterior-lateral to an LVM representation at the border of TO1.

Two cortical areas (TO1 and TO2), each containing a representation of contralateral space, were identified in lateral–temporal cortex along the medial–temporal gyrus, anterior to LO2 (Amano et al. 2009). The posterior border of TO1 was shared with the anterior–lateral border of LO2 at an LVM. TO1 and TO2 were separated by an UVM representation. TO2 extended anteriorly to an LVM representation. In a subset of subjects, the LVM of TO1 appeared discontinuous with the LVM of LO2, which might be consistent with an alternative parcellation of the retinotopic representation of the medial–temporal lobe described by Kolster et al. (2010). However, for consistency, we applied the parcellation scheme of Amano et al. (2009) for all of our subjects.

Parietal ROIs. Seven topographically organized areas (IPS0-5 and SPL1) were identified in the posterior–parietal cortex (Konen and Kastner 2008). Each contained a representation of the contralateral visual field and was separated from neighboring areas by reversals in the progression of the polar angle representation. The posterior–ventral border of IPS0 (also referred to as V7 in some studies) was formed by an UVM shared with V3A/B. The dorsal–anterior border of IPS0 was formed by an LVM shared with IPS1. IPS1 and IPS2, separated by an UVM, were located in the posterior part of the IPS. The dorsal–anterior border of IPS2 was formed by an LVM shared with IPS3. IPS3 and IPS4, separated by an UVM, were located in the anterior-lateral branch of the IPS. Starting at the anterior-lateral extent of IPS4 on an LVM, IPS5 extended toward the intersection between the IPS and the postcentral sulcus, ending at an UVM. SPL1 branched off the most superior areas of the IPS at an LVM and extended into the superior parietal lobule ending at an UVM.

Frontal ROIs. One frontal area (hFEF) was defined as a region of contralateral preference within human FEF (Kastner et al. 2007), although strict topography within this area was unclear. The hFEF was located near the junction of the superior branch of the pre-central cortex and the caudal superior frontal sulcus. In this study, we did not include another frontal cortex region, PreCC/IFS, reported in our previous study (Kastner et al. 2007) because it showed a large degree of variability across subjects, although some indication of this region was apparent in the group-averaged phase map displayed in Figure 4C (arrowheads).

Atlas Generation

Two types of visual probabilistic atlases were generated: a surface-based atlas (SBA) and a volume-based atlas (VBA). In order to transfer the subject-specific ROIs to a standardized coordinate system, we normalized each individual structural volume to a template in one of the 2 standard spaces as outlined below.

Surface-Based normalization. The reconstructed cortical surface was individually warped to the Buckner40 template in Freesurfer (Fischl, Sereno, Tootell et al. 1999) and then resampled in SUMA using an icosahedral shape to generate a standard mesh with a constant number of co-registered nodes (Argall et al. 2006). Subsequently, ROIs were converted from individual surface space to the standard-mesh surface using nearest-neighbor interpolation.

Volume-Based normalization. The individual high-resolution structural volume was spatially normalized to a standard template in MNI space (Collins et al. 1994) using a nonlinear transformation implemented by FSL's FNIRT (Andersson et al. 2007). The nonlinear transformation parameters were then applied to the individual volume ROIs projected from the surface.

Full and maximum probability maps. The following description is for the SBA, and thus refers to "nodes" on the cortical surface. The same algorithm was applied to the VBA, in which case "nodes" can be replaced by "voxels."

After normalization to standard space, corresponding ROIs from every subject were superimposed. For each ROI, a full probability map (FPM) was generated by dividing, at each particular node (i.e., coordinate), the number of times that location belonged to that ROI by the number of subjects included for that ROI. Hence, the probability values represent the likelihood that any node in the SBA would be classified as part of a given visual area.

Next, a maximum probability map (MPM) was calculated for each node by comparing the probabilities of all areas at that node and assigning the node to the area with the highest probability. To avoid extensive spreading of the MPM into regions of cortex that had low probabilities for all possible ROIs, we first added up the probability values for a node across all ROIs (inclusion) and compared this sum to the probability of that node being outside our visually defined areas (exclusion). If the probability of inclusion exceeded exclusion, the node was determined to be in a visual area; otherwise, it was discarded from the MPM. For each included node, the probability values were compared across ROIs and the node was assigned to the most likely ROI (Fig. 3*A*).

Group-averaged phase map. To complement the probabilistic atlases, which were created based on the overlap of discrete ROIs within standardized space, we also generated a group-averaged phase map for the retinotopy and memory-guided saccade tasks. Phase values for individual subjects were manually shifted and scaled to account for differences in stimulation parameters. The resulting phase values were then transformed into standard surface space. For each node in standard space, we calculated the circular mean and variance of the phase values across subjects.

Atlas characterization

ROI size. The average regional surface area for the subject-specific surface ROIs and the corresponding MPM ROIs of the SBA was measured and compared with each other in the left and right hemispheres, separately. As there were no significant differences across hemisphere (see Supplementary Fig. 5), we present data averaged over corresponding ROIs in the 2 hemispheres for this, and all subsequent analyses. A similar quantification of ROI size in volume space was performed for subject-specific volume ROIs and the corresponding MPM ROIs of the VBA.

Peak probability value. The peak probability was defined as the highest value in the FPM across all nodes for a given ROI.

Central tendency. To quantify the overlap between ROIs in the MPM and FPM, we compared the overall probability distribution (P_o) for the FPM of a given ROI with the mean probability distribution (P_m) for all nodes of the MPM of a given ROI. This measure is referred to as the central tendency (Eickhoff et al. 2007), defined as:

$$P_{i,j} = \frac{P_{m,i}}{P_{o,j}}, \quad i = 1, \ldots, 25, \; j = 1, \ldots, 25$$

where $P_{m,i}$ is the average full probability across all nodes of the ith ROI in the MPM and $P_{o,j}$ is the average full probability across all non-zero nodes in the jth FPM. This yielded a central tendency matrix (25×25), in which many off-diagonal elements were expected to be zero (e.g., we do not expect any overlap between the FPM of V1v and the MPM of hFEF). A high $P_{i,j}$ (e.g., >1) consequently indicates that the ith ROI in the MPM is at a central location with respect to the jth ROI in the FPM, whereas a small $P_{i,j}$ (e.g., <1) indicates overlap at a more peripheral location.

Blurring metric. As described above, we generated the FPM by superimposing the corresponding ROIs from individual subjects in standard space. If ROIs from all subjects cover exactly the same nodes in standard space, the pooled volume (i.e., total region with non-zero values in the FPM) will be equal to the individual volumes. Conversely, if the nodes of an ROI vary widely across subjects, the pooled volume will be substantially larger than the individual volumes. We quantified the expansion of the ith ROI using a blurring metric (Fischl, Sereno, Tootell et al. 1999), defined as

$$V_i = 100\% \times \frac{A_{i,\text{pooled}} - \bar{A}_i}{\bar{A}_i}$$

where $A_{i,\text{pooled}}$ is the pooled volume of the ith ROI across all subjects and $\bar{A}_i$ is the mean volume of the ith ROI across all subjects. This measure was expected to be highly correlated with the peak probability value; an ROI with small blurring metric, and thus high overlap across subjects, will have a large peak probability value. As atypical subjects, in terms of the anatomical location of their ROIs, may affect the pooled volume, we also calculated the blurring metric after first excluding portions of the pooled volume that overlapped with fewer than 5% of all subjects.

Anatomical variability. The probabilistic atlases of functionally defined regions capture variability both in the functional–anatomical correspondence across subjects (i.e., the consistency of a given ROI location with respect to major gyri and sulci), as well as the ability of the spatial normalization algorithm to align the anatomy of individual subjects (i.e., the alignment of gyri and sulci across subjects). Since the functional–anatomical variance is confounded with the anatomical variance, the anatomical variance may affect the FPM and peak probability values mentioned above. For example, poor alignment of certain gyri and sulci in standard space will lead to poor overlap of nearby functional ROIs in the vicinity of those structures. Anatomical variance is reflected in the mutable location of gyri and sulci during normalization, which we quantified as the variance of the gyral-

sulcal convexity across subjects in standard surface space (Fischl, Sereno, Tootell et al. 1999).

Atlas validation

Leave-one-out validation. To validate the FPM for use with novel subjects, we calculated the central tendency metric (see above) between ROIs in the FPM and ROIs defined in single-subjects. For each subject, we regenerated the FPM (and MPM, see below) after first excluding that subject from the atlas generation procedure. We then calculated the central tendency metric between every ROI in the leave-one-out FPM with every subject-specific ROI. To assess significance, we compared the mean central tendency across subjects for the corresponding ROIs in the subject-specific space and the leave-one-out FPM with the central tendency for all other FPM ROIs.

To validate the MPM for use with novel subjects, we compared the proportion of overlap between ROIs in the leave-one-out MPM and ROIs defined in single-subjects. Proportion overlap was determined with respect to (i.e., the denominator) the volume of the subject-specific ROIs, although using the volume of the MPM ROI yielded similar results. To assess significance, we compared the mean overlap across subjects for corresponding ROIs in the MPM and the subject-specific map with the overlap for all other subject-specific ROIs. A complementary analysis comparing overlap with the corresponding ROI and all other ROIs in the MPM yielded similar results.

Phase histograms. For each subject, we overlaid the leave-one-out MPM excluding that subject and the subject's individual phase maps from the localizer scans. To define the visual field coverage for each ROI in the MPM, we extracted the phase values from the memory-guided saccade task (IPS0-5, SPL1, and hFEF) or the retinotopy task (all other ROIs). For a given ROI, the total amount of the coverage from all subjects was concatenated and converted into a polar histogram. These data depict the probability of coverage of each part of the visual field for a given MPM ROI projected to a novel subject.

Resting-state functional connectivity. Functional connectivity, defined as the temporal correlation between spatially remote areas (Friston et al. 1993), is a useful metric for assessing large-scale cortical organization (Cohen et al. 2008; Yeo et al. 2011). However, recent evidence indicates that inaccurate ROIs can have a detrimental effect on connectivity estimates (Smith et al. 2011), particularly in resting-state functional connectivity. In contrast to parcellating functional imaging data based on a structure-based atlas (e.g., automated anatomical labeling template; Tzourio-Mazoyer et al. 2002), which may not accurately reflect the functional subdivisions of cortex, the MPM in this study provides functionally defined areal boundaries. These functional divisions can be used to extract the time series from visual ROIs for functional connectivity analysis. For 12 subjects, the mean time series from each run was extracted from each ROI. For each hemisphere, inter-regional functional connectivity was calculated as the temporal correlation for all pairwise ROIs. Subsequently, correlation values were averaged across both hemispheres and the 4 resting-state runs, and Fisher transformed. For this analysis, ROIs were defined from the SBA, VBA, or subject-native space. Furthermore, the SBA and VBA were re-created in a leave-one-out procedure by excluding the test subject (see above). We excluded ROIs that did not yield a sufficient number of voxels in both atlases at the resolution of the resting-state functional data.

Results

We generated a probabilistic atlas of 25 topographic maps covering 22 visual areas of the adult human brain (Table 1, Fig. 1 and Supplementary Figs 1–3) in 2 standard spaces. Below, we first describe the atlas generation process and make some qualitative and quantitative comparisons of the SBA and VBA. We then validate the use of the atlases with novel subjects using a leave-one-out cross-validation method.

Atlas Generation

Full Probability Map

We defined 25 topographic regions in individual subjects based on the representation of visual space as obtained from standard retinotopic mapping and memory-guided saccade mapping. Data from individual subjects were transformed into one of the two standard spaces: the Buckner40 standard surface space (Fischl, Sereno and Dale 1999) or MNI volume space (Collins et al. 1994). Within the standard space, data from individual subjects were superimposed and each ROI was delineated as a probability cluster, with each node (surface space) or voxel (volume space) reflecting the likelihood of being assigned to that ROI across subjects. The FPM captures the variance of ROI position across all subjects, with higher values representing regions of common overlap. An example probability map of V1d is displayed in both the standard surface (Fig. 2*A*) and volume (Fig. 2*B*) spaces. The color-coded nodes in the SBA (or voxels in the VBA) denote the likelihood of that node being assigned to V1d across our pool of subjects. In general, higher probabilities are located more centrally within the full distribution. The full range of possible probabilities is 0 to 100%, although there is a large variability across the ROIs. For example, the early visual area V1d shows a peak probability of 100%, whereas the high-order area IPS4 shows a peak probability of ~44% for the SBA.

Maximum Probability Map

Whereas the FPM captures the variance of ROI position across all subjects, the MPM, with each point in standard space assigned to the most probable region, provides a summary of the topographic organization across the population. The black line in Figure 2 denotes the border of the MPM for V1d. Because the MPM is a function of the FPMs for all ROIs (see below) and the FPM of neighboring ROIs overlap to some extent, the MPM is necessarily smaller than the FPM for any given ROI.

The algorithm for obtaining the MPM is schematically presented in Figure 3*A*, with 2 hypothetical ROIs shown in red (region R1) and blue (region R2). In this example, for any one voxel *i*, the probability of being assigned to either region R1, region R2, or outside of all defined topographic regions is 35, 25 and 40%, respectively. Clearly, the total within visual area probabilities (R1 + R2 = 60%) shows a higher probability than the outside visual area probability (40%). Comparing the probabilities for region R1 with region R2 directly (35 vs. 25%) leads to a final assignment of this voxel to region R1 in the MPM.

The MPM was generated separately for the standard surface (Fig. 3*B*) and volume (Fig. 3*C*) spaces. The topological organization and anatomical locations of the visual areas from the MPM are consistent with the topography observed for individual subjects (compare Fig. 3*B* with Fig. 1) (Silver and Kastner 2009; Wandell and Winawer 2011). The consistency between ROIs in the atlas MPM (and FPM) and subject-specific ROIs is quantified below (see *Atlas validation*).

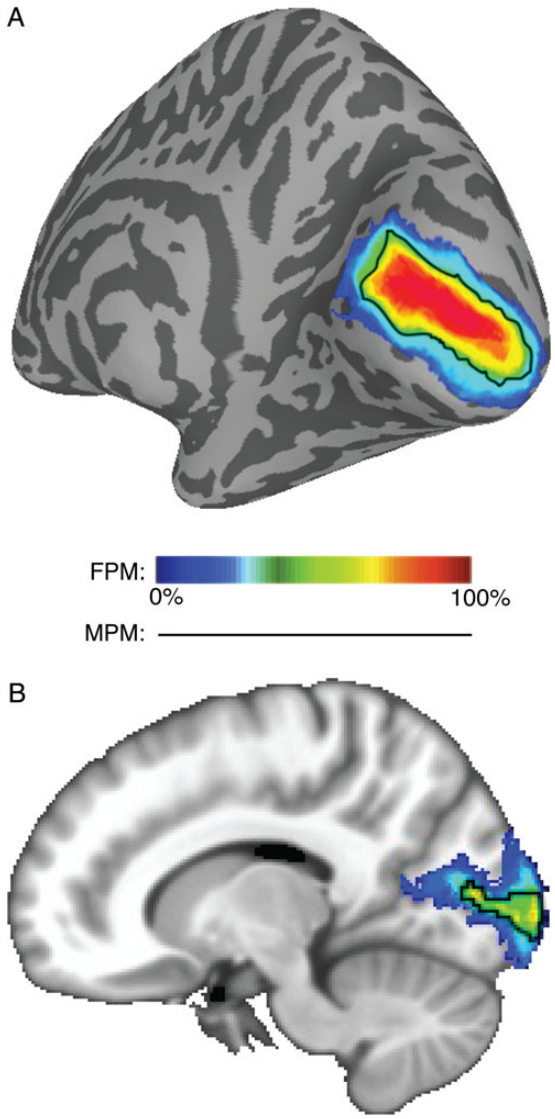

Figure 2. An exemplary FPM of the right hemisphere V1d. The color-coded nodes in the SBA (*A*) and voxels in the VBA (*B*) denote the probability of that node or voxel being assigned to the right V1d across subjects ($n = 50$). The probability gradually increases from blue to red indicated by the color scale. In both panels, higher probabilities are located more centrally within the full distribution accounting for the majority of the variance in anatomical location across subjects (see central tendency measure for more details). For comparison, the black line denotes the border of the MPM for V1d, which is a function of the FPMs for all ROIs (see Fig. 3).

Group-Averaged Phase Map

The MPM and FPM described above were generated from the overlap of discrete ROIs from many subjects in standard space. As a comparison, we also generated group-averaged phase maps for the retinotopy (Fig. 4A, *B* and Supplementary Fig. 4) and memory-guided tasks (Fig. 4C). These maps depict the polar angle phase values associated with each node in the standard surface space averaged across subjects. Only those nodes that have a variance less than or equal to 0.80 (retinotopy task, Fig. 4A,*B*) or 1.20 radians (memory-guided saccade task, Fig. 4C; retinotopy task, Supplementary Fig. 4) are displayed. In addition, borders between adjacent ROIs derived from the MPM are displayed for comparison (see Fig. 3*B*).

Most notably, regions of cortex showing the most consistent phase values across subjects (i.e., those nodes with low variance and which are displayed in Fig. 4) are well captured by the MPM. Exceptions to this observation in early visual cortex for the memory-guided saccade task (Fig. 4C) are expected, given that this task specifically avoids stimulation of the center ~10° of space. Likewise, exceptions in the parietal cortex for the retinotopy task (Fig. 4A) are not surprising, given that the stimulus parameters for this task are not optimized for mapping these regions. Regardless, consistent phase representations in parietal regions covered by the MPM were evident when using a less conservative threshold (1.20 radians, Supplementary Fig. 4).

Although the borders of Figure 4 are derived from the MPM, and not the group-averaged phase map itself, there is generally good alignment between the expected phase reversals and the group-averaged phase map. This was especially true for lower-order regions, such as V1–V3. Average phase values for higher order regions, such as LO1-TO2, VO2-PHC2, and IPS3-5, are generally located near the HM, indicating a clear contralateral bias in these areas, but more variability with respect to the precise location of the phase reversals with respect to the underlying anatomy. This is consistent with the quantitative analysis of the FPM and MPM presented below.

It is worth noting that the topographic region of the frontal cortex called PreCC/IFS (2007), which was excluded from the probabilistic atlas due to high inter-subject variability, was apparent in the group-averaged phase maps (see arrowheads in Fig. 4C). Finally, the apparent topographic map on the medial surface (see arrowheads in Fig. 4*B*) likely represents activity from the thalamus (Schneider et al. 2004) that is being captured by the cortical surface models. We verified that this was the case by visual inspection in individual subjects.

Atlas Characterization

ROI size

Figure 5 illustrates the average size and variance of the subject-specific ROIs and the MPM ROIs from the SBA (ROI surface area, Fig. 5A) and VBA (ROI volume, Fig. 5*B*). The corresponding data separated by hemisphere are shown in Supplementary Figure 5. ROI size varied widely across different ROIs, but the pattern did not significantly differ across hemisphere for either the single-subject (surface: $P = 0.50$; volume: $P = 0.46$, paired *t*-tests) or the MPM (SBA: $P = 0.74$; volume: $P = 0.42$, paired *t*-tests). As such, we present data averaged over corresponding ROIs in the 2 hemispheres for this and all subsequent analyses. Linear correlation analysis across all ROIs indicates that the amount of ROI size and variability from the 2 MPM atlases showed a similar trend as seen for the subject-specific ROIs (SBA: $r = 0.81$, $P << 0.001$; VBA: $r = 0.72$, $P < 0.001$).

Figure 5C shows a direct comparison between the MPM ROI size of the SBA and VBA as a percentage of the single-subject ROI size. For every ROI, the size of the MPM ROI in the SBA was closer to that of the single-subject ROI size than for the VBA. This difference in MPM ROI size as a percentage of the single-subject ROI size for the SBA and VBA was highly significant ($P << 0.001$, paired *t*-test). Still, the area of some ROIs from the SBA MPM showed considerable departures from the mean area for the subject-specific ROIs, such as TO2, PHC1/2, IPS4, IPS5, SPL1, and hFEF. This reflects the fact that the MPM highlights the region of maximal overlap between subjects, which is smaller for ROIs showing larger anatomical location variability across subjects. This observation is further explored in the analyses presented below.

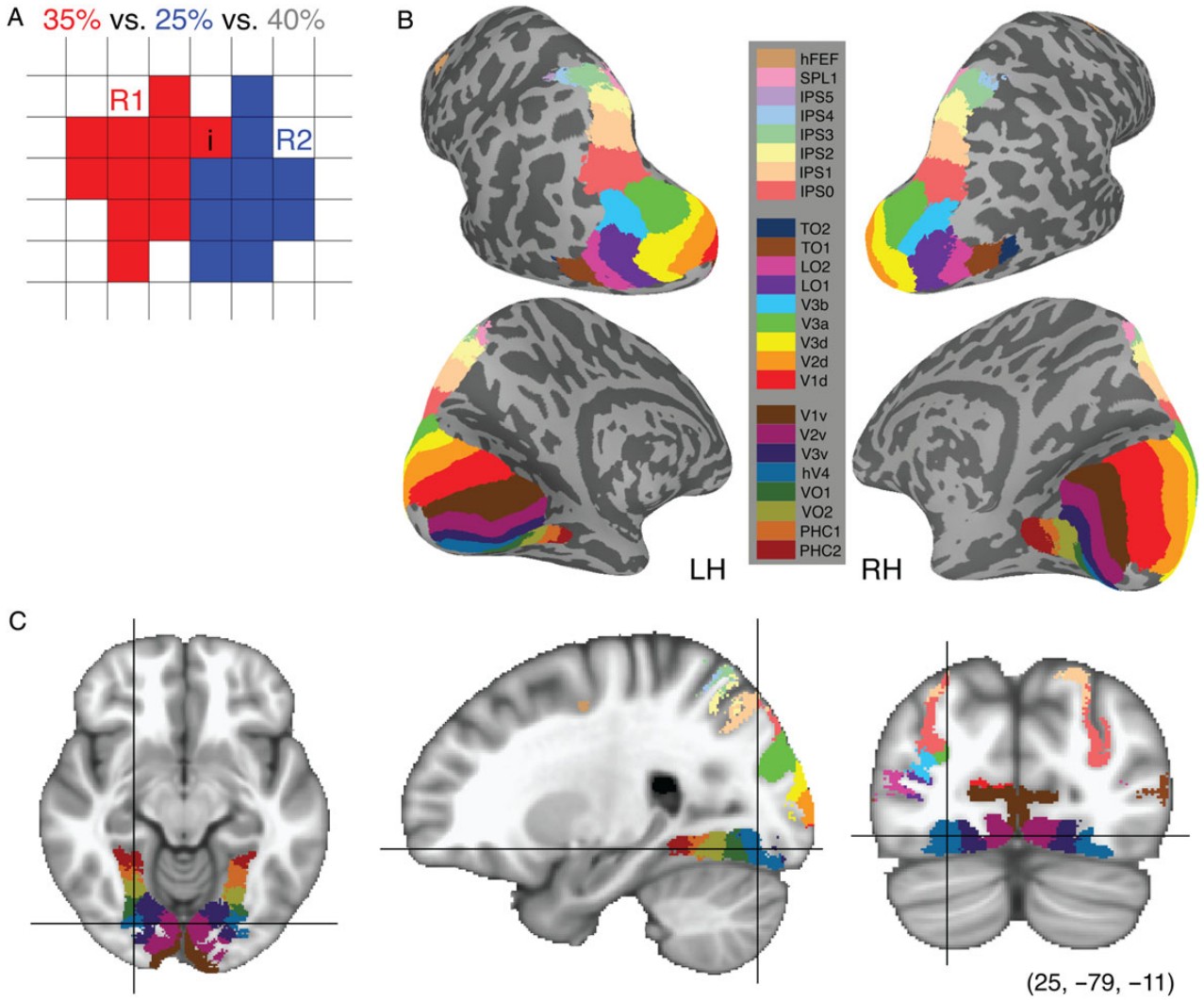

Figure 3. MPM of visual topography. (*A*) Schematic presentation of the algorithm for generating the MPM. For the ith element, the probability of being assigned to region R1 (red), region R2 (blue) and outside visual topography (white) is 35, 25 and 40%, respectively. First, we combined the probability arranged in visual topographic areas together and compared with the outside one. Then choosing the maximum probability over all candidates within visual topography takes the ith element to be assigned to region R1. MPMs are displayed in both surface (*B*) and volume (*C*) space. Each color-coded area denotes a specific visual ROI. The surface MPM (*B*) shows the same overall structure as seen in individual subjects (see Fig. 1). The color map is the same for both surface and volume space.

Peak Probability Value

The peak probability value from the SBA and VBA (Fig. 6) averaged over 2 hemispheres showed large variability across ROIs. For example, the peak probability changed from ~100% in the early visual areas (e.g., V1v) to ~60% in the ventral medial visual areas (e.g., PHC2) to ~40% in the anterior parietal cortex (e.g., IPS5) for the SBA. Consistent with multiple metrics outlined below, this finding indicates that the variability in the alignment of ROIs in standard space increased for more anterior regions. Furthermore, we found that peak probability values from the SBA were globally higher than those from the VBA ($P << 0.001$, paired t-test) suggesting better alignment of ROIs across subjects in the standard surface space.

Central Tendency

We characterized how well a given ROI in the MPM of the SBA (Fig. 7A) and VBA (Fig. 7B) aligned with the full probability distribution using a central tendency metric. Both figures show that the highest central tendency values were always located along the diagonal of the MPM ROI × FPM ROI matrix, with decreasing values away from the diagonal. This indicates that all the ROIs in the both MPMs were located at the center of the corresponding FPM. In contrast to ventral–temporal and dorsal–lateral visual areas, some parietal visual areas (e.g., anterior regions IPS3-5 and SPL1) exhibited more spread to off-diagonal elements, although even in these cases, the highest values were still consistently located along the diagonal. This implies that one parietal ROI in the MPM may be located at the periphery of the FPM of neighboring areas. This spread was most prominent in the VBA, compared with the SBA and is consistent with the observations from the peak probability value presented above indicating less consistency in the alignment of ROIs in standard space for anterior regions.

Blurring Metric

Figure 8A shows a comparison of the blurring metric for each ROI in the SBA and VBA. The blurring metric indicates the extent of expansion of the pooled ROI size over all subjects relative to the

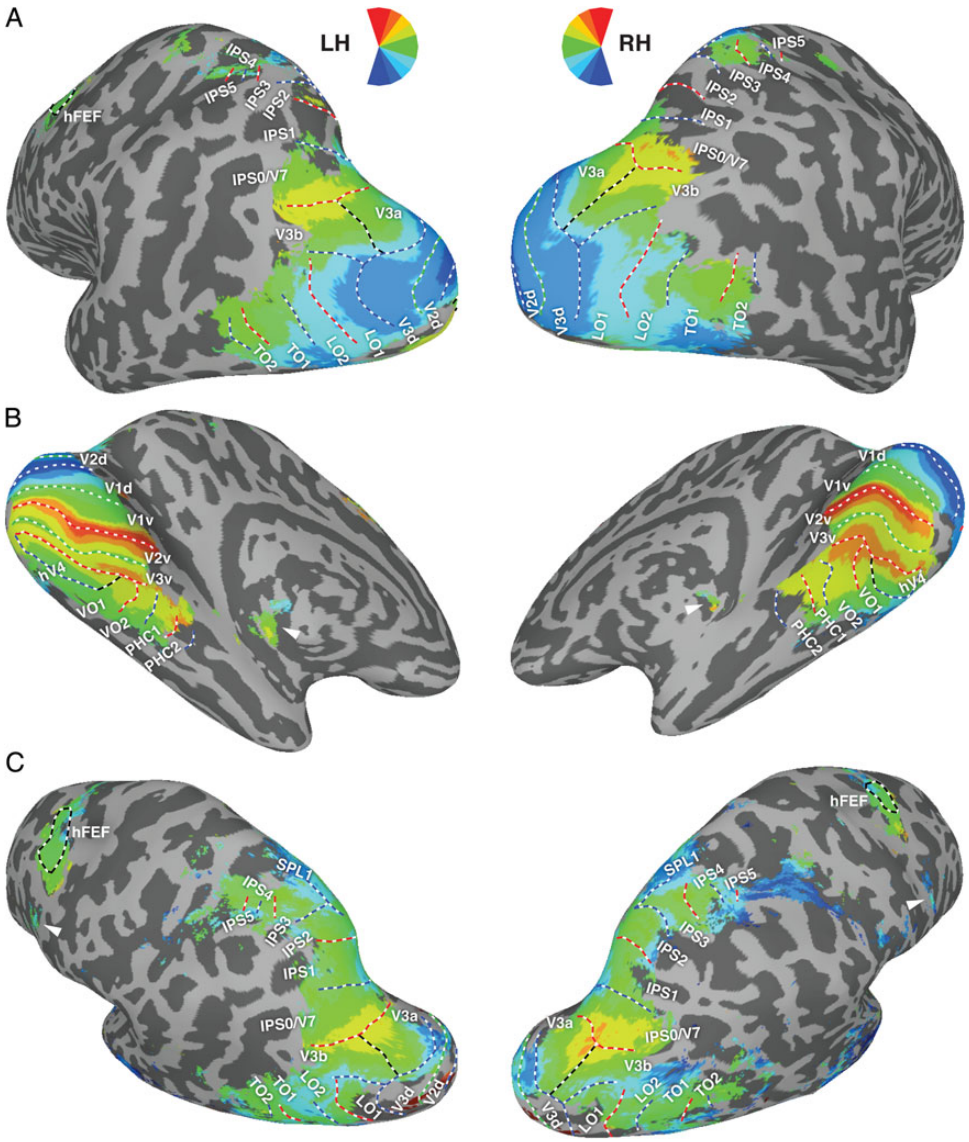

Figure 4. Group-averaged phase maps and comparison with MPM. Average phase values across subjects for dorsal–lateral (*A*) and ventral–temporal (*B*) regions obtained from the retinotopy task, and parietal and frontal regions (*C*) obtained from the memory-guided saccade task. The color code indicates the region of the visual field to which each surface node responded best, on average, across subjects. Data are only shown for nodes with a variance less than or equal to 0.80 (retinotopy task, *A* and *B*) or 1.20 radians (memory-guided saccade task, *C*; see also Supplementary Fig. 4 for retinotopy task). ROI labels and borders between neighboring areas are derived from the MPM (see Fig. 3*B*). White lines denote area boundaries, defined in individual subjects as phase reversals at or close to the upper vertical (dashed red), lower vertical (dashed blue), or horizontal (dashed green) meridians. Dashed black lines indicate borders based on eccentricity representations or the outline of hFEF. Note that because the borders are derived from the MPM, the dashed colored lines indicated the expected phase reversals, not phase reversals derived from the group-averaged phase maps themselves. Arrowheads in (*B*) indicate activity that is likely derived from the thalamus (Schneider et al. 2004). Arrowheads in (*C*) indicate the region that is likely the PreCC/IFS, previously reported by Kastner et al. (2007).

mean ROI size across subjects. It also reflects the functional–anatomical variance across the ROIs to some degree (see below). A blurring metric value of zero for a given ROI indicates perfect overlap for that ROI across subjects in standard space; high values indicate more variability in the standard-space position of an ROI across subjects. We found relatively low blurring metric values in early visual areas (e.g., V1v), relatively higher values in the lateral–occipital cortex (e.g., LO1/2), and much higher values in the anterior parietal cortex (e.g., IPS4). Consistent with previous analyses (e.g., peak probability value, Fig. 6), the lower blurring metric values for posterior ROIs indicate that there was relatively more consistent alignment of posterior regions compared with anterior regions in standard space. As expected, the blurring metric showed an inverse correlation with the peak probability value (SBA: $r = -0.96$, $P << 0.001$; VBA: $r = -0.87$, $P << 0.001$).

In every case, the blurring metric for a given ROI was lower for the SBA compared with the VBA, leading to a highly significant difference ($P << 0.001$, paired *t*-test). Again, consistent with the analysis of peak probability, this suggests that the standard surface space provided better alignment of topographic ROIs across subjects.

Given that the blurring metric includes a measure of the pooled ROI size across all subjects, it may be sensitive to atypical anatomical locations of an ROI in a particular subject. To verify that this did not contribute to our results, we recalculated the

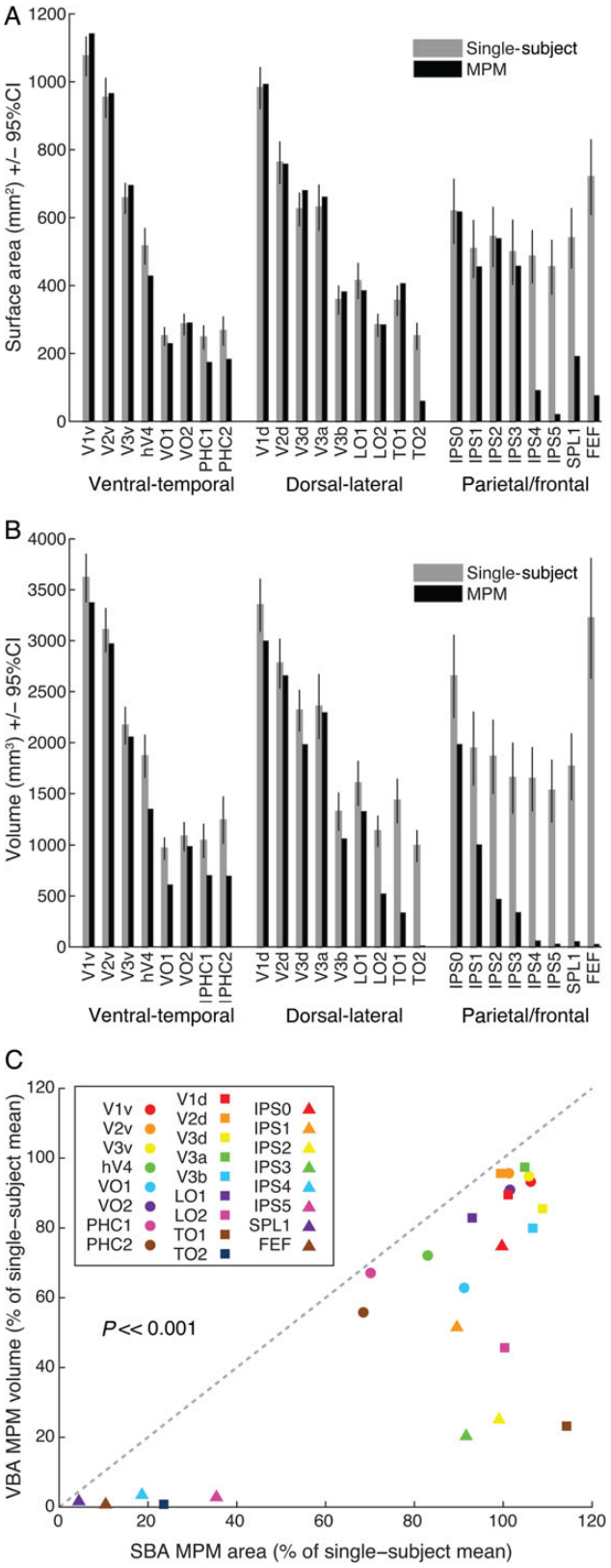

Figure 5. Comparison of subject-specific ROI size with that of the MPM in surface and volume space. (*A*) Comparison of the surface area of subject-specific ROIs (gray bars) and the average surface area of the SBA MPM ROIs (MPM, black bars). (*B*) Comparison of the volume of subject-specific ROIs (gray bars) and the VBA MPM ROIs (black bars). In both cases, the largest discrepancies were observed for higher-order topographic regions. Error bars denote 95% confidence intervals. (*C*) A direct comparison of the MPM ROI size for the VBA versus the SBA, presented as a proportion of the average subject-specific ROI size. Compared with the VBA, MPM ROI size for the SBA better reflected the subject-specific ROI size ($P << 0.001$, paired *t*-test). Data for individual hemispheres are presented in Supplementary Figure 5.

blurring metric after first eliminating portions of the pooled volume that overlapped with fewer than 5% of all subjects (Fig. 8*B*). Although this lead to overall lower blurring metric values, it did not change the pattern observed across ROIs or between the SBA and VBA.

Anatomical Variance

The alignment of topographic regions from individual subjects within standard space is a function of both the functional–anatomical correspondence across subjects (i.e., the consistency of a given ROI location with respect to major gyri and sulci), as well as the ability of the spatial normalization algorithm to align the anatomy of individual subjects (i.e., the alignment of gyri and sulci across subjects). Thus, we explored the relationship between anatomical and functional variance contributing to the probabilistic atlas.

For the SBA, individual cortical surfaces were warped to a standard surface space (Buckner40 template; Fischl, Sereno, Tootell et al. 1999). Figure 9*A* shows the mean convexity across subjects in standard surface space. In general, the major sulci and gyri were well aligned across all subjects. Independent of functional variability, the variance measured by cortical convexity allows us to quantify anatomical variability at a node-wise level. Figure 9*B* shows the variance in convexity across subjects in standard surface space. In general, lateral–occipital, –parietal, and –anterior prefrontal cortex showed relatively high anatomical variance, while ventral–temporal, medial–occipital, and medial–prefrontal cortex showed relatively low anatomical variance. Consistently, the mean convexity variance of each visual ROI showed a similar pattern (Fig. 9*C*), with higher anatomical variability in middle temporal and parietal regions than near the calcarine and collateral sulci.

To a certain extent, anatomical variance may predict functional variance. To test this, we measured the correlation between the convexity variance and peak probability value (Fig. 9*D*) and blurring metric (Fig. 9*E*) across the ROIs of the SBA, and found that the two correlation coefficients were highly significant ($r = -0.46$, $P = 0.02$; $r = 0.56$, $P = 0.004$, respectively). The relationship between convexity, blurring metric, and peak probability values suggests that higher anatomical variability leads to less overlap of ROIs across subjects in standard space.

It is important to note that anatomical variance within any given standard space is a function of the algorithm used to transform individual subject data into that space. Future improvements in anatomical correspondence between individual subjects would likely improve the quality of functional atlases such as our own.

Atlas Validation

Individual ROI and Atlas Overlap

Generally speaking, there are two ways in which the atlas presented above could be applied to novel subjects (i.e., those who were not included in the atlas generation process). In an exploratory, data-driven analysis, one may wish to determine the most probable location(s) with respect to visual topography of some functional activation defined in an individual subject.

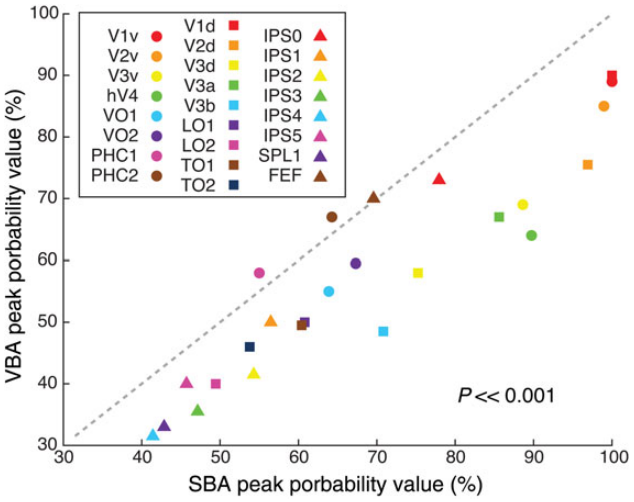

Figure 6. Peak probability values for the FPM. The peak probability value was calculated for each ROI in both the SBA and VBA. In general, this value was higher in SBA than VBA across all ROIs ($P << 0.001$, paired *t*-test).

Alternatively, one may wish to test an *a priori* hypothesis about the function of a particular visual topographic region. The FPM is useful for exploratory analyses or interpreting patterns of functional activation (Eickhoff et al. 2007), whereas the MPM is useful for defining ROIs for hypothesis-driven questions (Eickhoff et al. 2006). To validate the use of the FPM and MPM for these applications, we used a cross-validation approach in which the atlases were regenerated after excluding a single test subject and then quantifying how well the atlas ROIs overlapped with the subject-specific ROIs of the test subject.

First, we address the question of whether a functionally defined region from a novel subject (e.g., V1d) would intersect best with the corresponding region in the leave-one-out FPM (e.g., V1d), compared with all possible regions of the leave-one-out FPM (e.g., V1v, V2d, etc.). To do so, we compared the correspondence between the FPM and single-subject ROIs using the central tendency metric. Figure 10 shows the mean central tendency for all pairwise comparisons of ROIs in the leave-one-out FPM (vertical axis) and subject-specific ROIs (horizontal axis). Higher central tendency values indicate better overlap. Mean central tendency values for corresponding ROIs did not differ

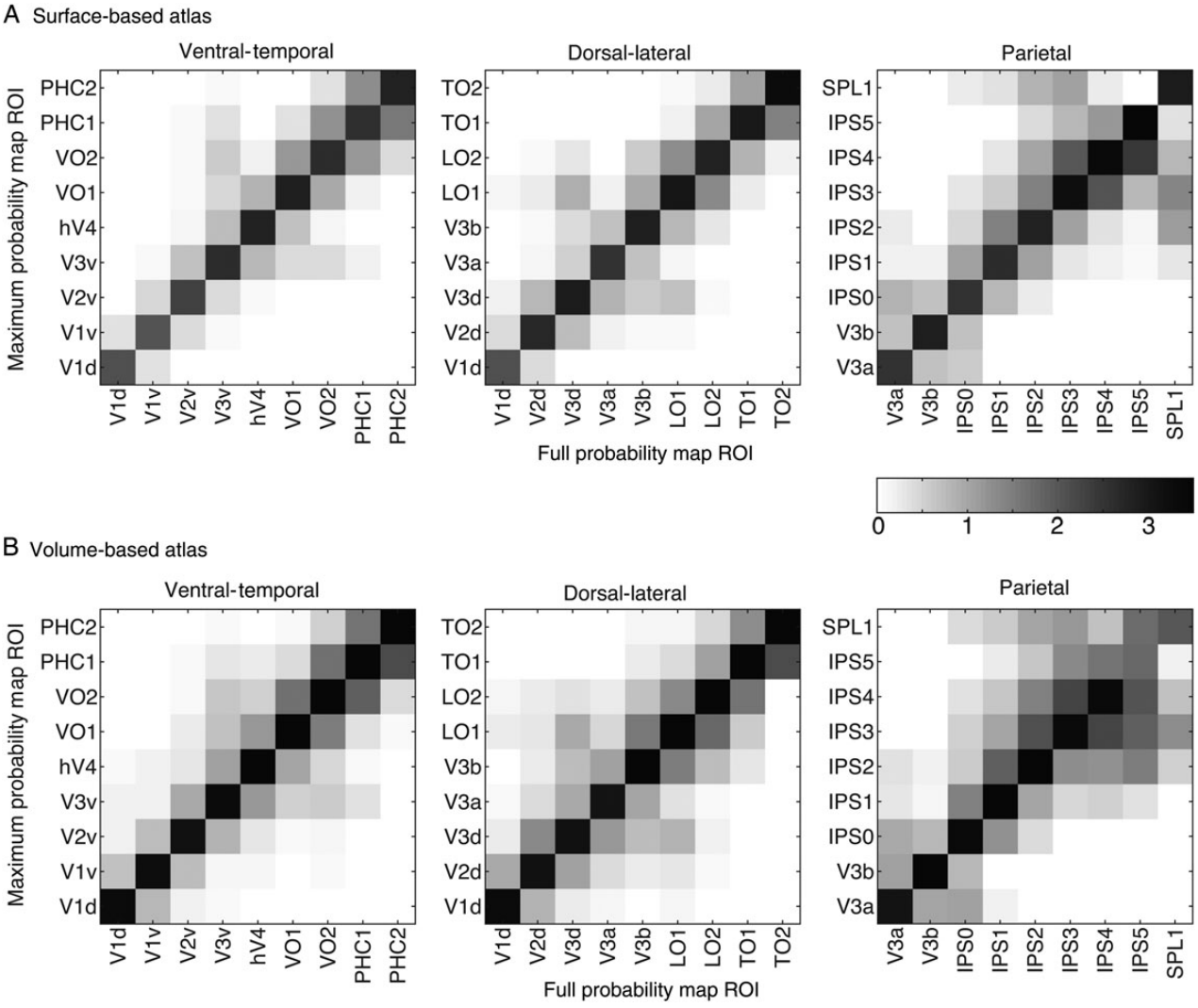

Figure 7. Central tendency metric in surface (*A*) and volume (*B*) based atlases. For all panels, the highest values consistently fall along the diagonal, with values gradually decreasing away from the diagonal. For convenience, data are divided into 3 groups of ROIs (ventral–temporal, dorsal–lateral and parietal areas). Note, however, that V1d is included with ventral–temporal ROIs, and V3a and V3b are included with parietal ROIs so that all neighboring ROIs (i.e., those that share a border) can be directly compared in at least one of the panels. The frontal region hFEF is not displayed because no other ROIs in the atlases border hFEF and thus we do not expect any non-zero off-diagonal values for hFEF.

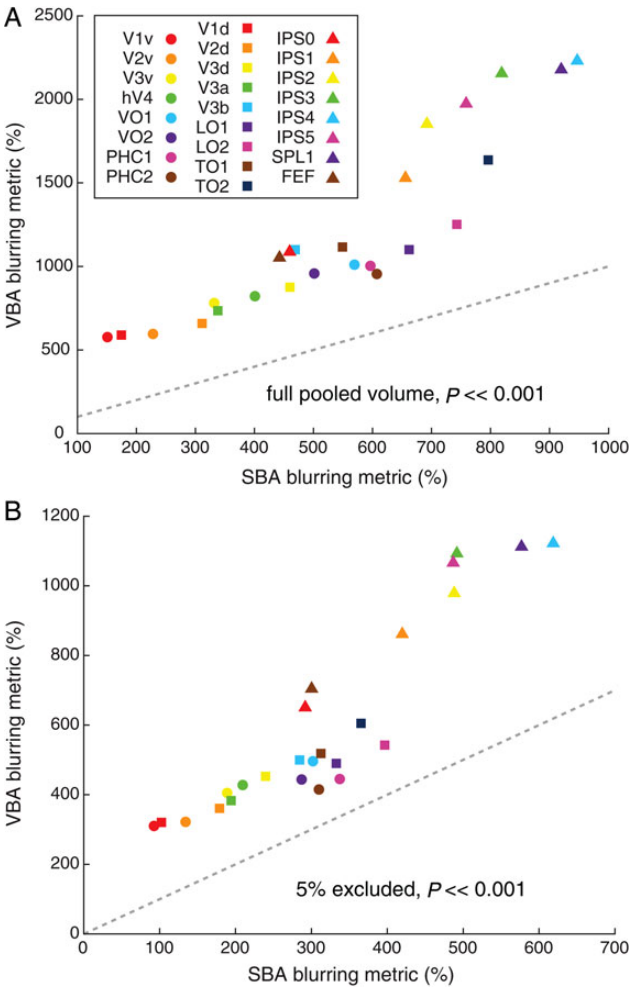

Figure 8. Blurring metric in SBA (*A*) and VBA (*B*). The blurring metric is a measure of how well ROIs from individual subjects overlap in the standardized space. As this metric may be sensitive to subjects with atypical ROI locations, we calculated the blurring metric using a pooled volume defined as the full extent of the FPM (*A*) and after first excluding regions that were covered by less than 5% of all subjects (*B*). In both cases, the blurring metric was always lower for the SBA and this difference was highly significant across all ROIs ($P << 0.001$, paired *t*-test).

significantly across the SBA ($M = 1.89$, $SD = 0.20$) and VBA ($M = 1.93$, $SD = 0.29$; $P = 0.45$, paired *t*-test). For both the SBA and the VBA, the highest values were always found for the comparison of corresponding ROIs (diagonal of Fig. 10). For each subject-specific ROI, we compared the central tendency for the corresponding ROI in the FPM with all other ROIs in the FPM (i.e., column-wise comparisons in Fig. 10) using Dunnett's correction for multiple comparisons following an ANOVA. For the SBA, the central tendency calculated between a subject-specific ROI and the same ROI in the atlas (i.e., diagonal of Fig. 10) was significantly higher than all other ROIs in the atlas, with the exception of IPS4 (confusable with IPS3;, i.e., higher but not significant [n.s.]) and IPS5 (confusable with IPS4, n.s.). The same was true for the VBA, with the exceptions being IPS3 (confusable with IPS4, n.s.), IPS4 (higher for IPS5, n.s.) and IPS5 (confusable with IPS4, n.s.). Thus, the FPM was a useful predictor of visual topographic regions in novel subjects, with slight local confusion (i.e., neighboring ROIs) in the anterior IPS. These confusions are likely due to the high anatomical variance across subjects in these regions (Fig. 9).

Next, we address the question of how well the leave-one-out MPM can be used to define visual topographic regions of interest in novel subjects. In other words, will an ROI in the MPM (e.g., V1d), when applied to a novel subject, overlap best with the same ROI in that subject (e.g., V1d) compared with all possible visual topographic regions in that subjects (e.g., V1v, V2d, etc.)? To address this question, we compared the proportion overlap between MPM ROIs and single-subject ROIs. Specifically, we calculated the proportion of a single-subject ROI volume that overlapped with each ROI of the MPM. In other words, overlap was quantified with respect to (i.e., the denominator) the single-subject ROI. Figure 11 shows the proportion overlap for all pairwise comparisons of ROIs in the leave-one-out MPM (vertical axis) and the subject-specific ROIs (horizontal axis). A direct comparison of the SBA and VBA revealed that the proportion overlap for corresponding ROIs was significantly higher for the SBA ($M = 0.41$, $SD = 0.23$) than for the VBA ($M = 0.22$, $SD = 0.16$; $P << 0.001$, paired *t*-test). For both the SBA and the VBA, the best overlap was usually found for the comparison of corresponding ROIs (diagonal of Fig. 11). For each ROI in the MPM, we compared the proportion overlap for the corresponding subject-specific ROI with all other subject-specific ROIs (i.e., row-wise comparisons in Fig. 11) using Dunnett's correction for multiple comparisons following an ANOVA. For the SBA, the proportion overlap calculated between a subject-specific ROI and the same ROI in the atlas (i.e., diagonal of Fig. 11) was significantly higher than all other ROIs in the atlas, with the exceptions being IPS4 (higher for IPS3, n.s.), and IPS5 (higher for IPS4, n.s.). The same was true for the VBA, with the exceptions being IPS3 (confusable with IPS4, n.s.), IPS4 (confusable with IPS2 and SPL1, n.s.; higher for IPS5, n.s.; significantly higher for IPS3, $P < 0.05$), and IPS5 (confusable with IPS1 and IPS2, n.s.; higher for IPS4, n.s.; significantly higher for IPS3, $P < 0.05$).

The results from the proportion overlap analyses demonstrate that the MPM was a useful predictor of visual topographic regions in novel subjects, with some local confusion (i.e., neighboring ROIs) for higher-order regions, especially in the anterior parietal cortex. As with the analysis of the FPM (leave-one-out central tendency, see above), these confusions and exceptions are likely due to the high anatomical variance across subjects in these regions (Fig. 9) and, in addition, the relatively small volume of these ROIs in the MPM (Fig. 5). Although there were more instances of confusion for the comparison of the MPM (proportion overlap) with single-subject ROIs compared with the FPM (central tendency), this should be expected given the necessary exclusion of information by converting the continuous FPM to a discrete MPM.

Overall, the results of the cross-validation analysis show that the visual topographic probabilistic atlases described here can be successfully used to interpret the location of functional activation in novel subjects or to define *a priori* estimates of visual topographic regions in individual subjects.

Phase Histograms

Although the probabilistic atlas we present is designed to provide information at the spatial scale of entire topographic ROIs, it is useful to consider how the atlas captures the more fine-grained polar coordinates of the visual field. To do so, we projected the leave-one-out MPM from the SBA onto the cortical surface of the excluded subject. For each ROI in the MPM, we extracted the phase values from the memory-guided saccade task (IPS0-5, SPL1, and hFEF) or the retinotopy task (all other ROIs). Phase values were concatenated across all subjects using the leave-one-out procedure to tally and converted into polar histograms,

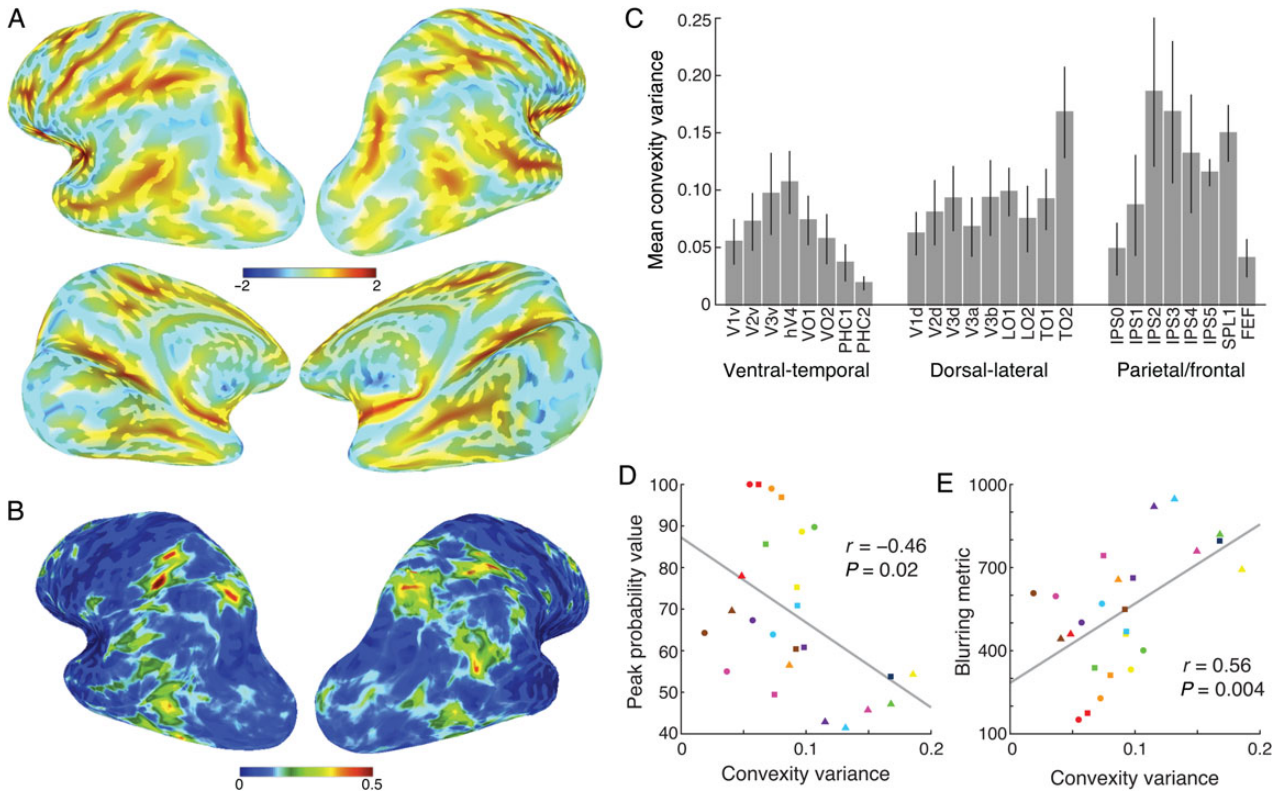

Figure 9. The effect of anatomical variance on the surface-based probabilistic atlas. Anatomical variance was quantified by sulci and gyri convexity. The nodal-based mean (*A*) and variance (*B*) of the convexity are shown on brain surfaces for visualization purposes. The ROI-based mean variance and standard error of the convexity for each ROI averaged across both hemispheres in MPM across the subjects is also shown (*C*). Significant correlations between mean convexity variance and peak probability value (*D*) and blurring metric (*E*) were observed across the ROIs. Marker conventions for individual ROIs are as in Figure 5.

separately for each hemisphere. As can be seen in Figure 12, all MPM ROIs projected to regions with a clear contralateral bias of visual field coverage. In addition, the ventral (Fig. 12*A*) and dorsal (Fig. 12*B*) portion of V1-V3 show clear biases toward the upper and lower contralateral quadrants, respectively, consistent with the representation of a single quadrant of the visual field in these regions (Sereno et al. 1995; DeYoe et al. 1996; Engel et al. 1997). Other expected visual field biases for higher-order regions based on previous reports from fMRI mapping studies were also apparent. The ventral–temporal regions hV4- PHC2 (Fig. 12*A*) all showed an upper-field bias (Larsson and Heeger 2006; Hansen et al. 2007; Arcaro et al. 2009; Kolster et al. 2010; Winawer et al. 2010). In contrast, LO1 and LO2 (Fig. 12*B*) showed a lower-field bias (Larsson and Heeger 2006; Kolster et al. 2010). Finally, the IPS regions IPS0-1 and SPL1 (Fig. 12*C*) showed some ipsilateral coverage, although this was still a small proportion in comparison with the contralateral coverage in these regions. Overall, these data provide further evidence that MPM is a useful predictor of visual topographic regions in novel subjects.

Resting-State Functional Connectivity

We evaluated the quality of the SBA and VBA using a resting-state fMRI dataset acquired from 12 subjects. We calculated functional connectivity between any two atlas-based visual ROIs as well between any two subject-specific ROIs. For this analysis, the SBA and VBA were recreated by leaving out the test subject (see above). The mean time series was extracted from each ROI before calculating inter-regional functional connectivity and then averaged across both hemispheres and sessions.

Given the fact that the SBA better preserved the visual topographic structure relative to the VBA, we hypothesized that functional connectivity matrix derived from the SBA would show a more similar pattern to one from the single-subject ROIs (i.e., in the subject's native space) than one from the VBA. Figure 13 shows 3 connectivity matrices for a representative subject (Fig. 13*A*–*C*) and for the group average (Fig. 13*D*–*F*) for the SBA (Fig. 13*A*,*D*), single-subject ROIs (Fig. 13*B*,*E*), and VBA (Fig. 13*C*,*F*). Globally, the connectivity pattern from both the SBA (individual: $r = 0.93$, $P << 0.001$; group: $r = 0.96$, $P << 0.001$) and VBA (individual: $r = 0.80$, $P << 0.001$; group: $r = 0.87$, $P << 0.001$) were significantly correlated with the single-subject ROIs, as measured by spatial correlation. However, we found the similarity between the connectivity patterns from the SBA and single-subject ROIs was significantly higher than those between the VBA and single-subject ROIs based on Meng's z-test (Meng et al. 1992) (individual: $z = 8.39$, $P < 0.001$; group: $z = 11.95$, $P < 0.001$). These results show that the MPM of the SBA is more representative of visual topography in individual subjects than that of the VBA.

Discussion

We describe a probabilistic atlas of topographically defined visual areas of the human brain. Twenty-five topographic regions, covering 22 visual areas (with V1–V3 separated into ventral and dorsal portions), were defined in individual subjects using standard mapping procedures. Data from individual subjects were normalized into one of the two standard spaces based on anatomical transforms: the Buckner40 standard surface space (Fischl,

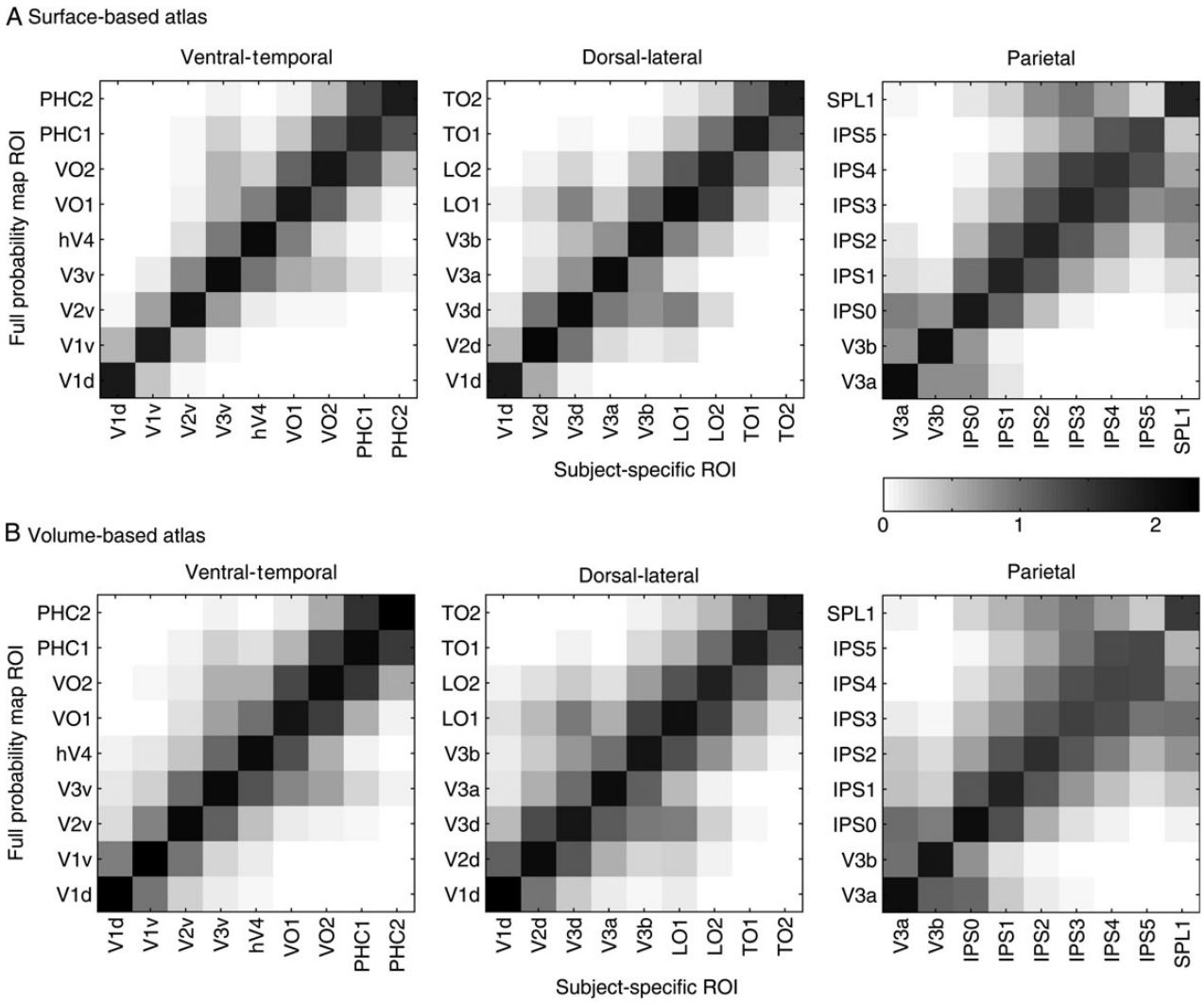

Figure 10. Leave-one-out validation of FPM. Central tendency calculated for all pairwise comparisons of ROIs in the leave-one-out FPM and ROIs defined in independent individual subjects for the SBA (A) and VBA (B). For example, V1v of leave-one-out FPM (*y*-axis) is compared with all subject-specific ROIs (*x*-axis) in the ventral–temporal portion of cortex from V1v to PHC2. For all panels shown, higher values consistently fall along the diagonal, with values gradually decreasing away from the diagonal. This analysis validates the use of the FPM for use with novel subjects that did not contribute to the atlas generation. Conventions are the same as in Figure 7.

Sereno, Tootell et al. 1999) or MNI volume space (Collins et al. 1994). The FPM captures the distribution of overlap across individual subjects for each ROI and characterizes the probability that any given position in the standard space would be classified as that ROI. In addition, the MPM provides an estimate of the ROI showing the most consistent overlap across subjects at each position within standard space relative to other ROIs in the atlas. Importantly, we validated the appropriateness of the atlas by comparing the overlap of the MPM with data from novel subjects in a leave-one-out cross-validation procedure. The best overlap between the MPM and the subject-specific ROIs was consistently between corresponding ROIs.

It should be noted that variability within any given probabilistic atlas is influenced by both the functional–anatomical alignment of regions across subjects (Hinds et al. 2008; Benson et al. 2012; Witthoft et al. 2013) and the quality of the anatomical alignment to the normalized space. Not surprisingly, multiple quantitative measures revealed that early visual areas (e.g., V1–3) were better aligned across subjects within the standard spaces relative to higher-order areas (e.g., IPS4/5). This does not simply reflect distance from V1. For example, peak probability and blurring metric values indicate that hFEF displays moderate inter-subject variability, and LO1/2 displays higher inter-subject variability than the more anterior TO1/2. Functional alignment was also better for regions of the ventral–temporal regions (e.g., PHC1/2) compared with dorso-lateral (e.g., TO1/2) and anterior parietal regions (IPS4/5). These results are at least partially explained by the increased anatomical variability in the anterior intraparietal sulcus and middle temporal cortex compared with the calcarine and collateral sulci (Fig. 9). They also highlight an important point regarding the interpretation of data from group-level analyses, in particular null results. If one observes a significant group-level effect in early visual cortex (e.g., V1d, V2d, and V3d), but not higher-order cortex (e.g., TO1 and TO2), it may be due to the poorer anatomical and functional alignment in the higher-order regions. As such, our atlas provides a voxel-wise quantification of the variance in spatial sensitivity across visual cortex that can guide the interpretation of group-level analyses.

The atlases provided here can be applied to novel subjects for both hypothesis-driven and data-driven analyses. In hypothesis-

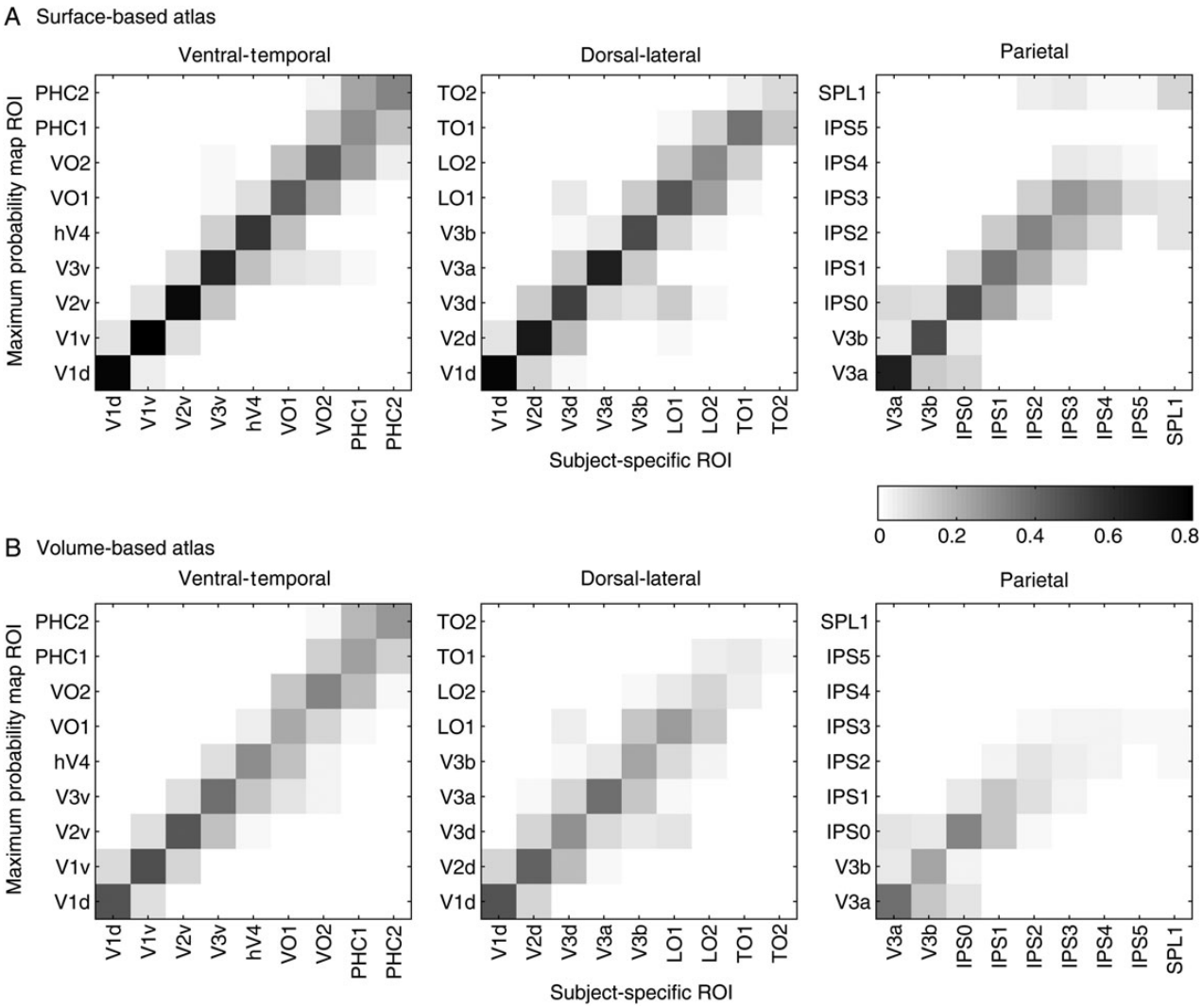

Figure 11. Leave-one-out validation of MPM. Proportion overlap calculated between all pairwise comparisons of ROIs in the leave-one-out MPM and ROIs defined in independent individual subjects for the SBA (A) and VBA (B). For example, V1v of leave-one-out MPM (y-axis) is compared with all subject-specific ROIs (x-axis) in the ventral–temporal portion of cortex from V1v to PHC2. For all panels shown, higher values mainly fall along the diagonal, with values gradually decreasing away from the diagonal. This analysis validates the use of the MPM for use with novel subjects that did not contribute to the atlas generation. Conventions are the same as in Figure 7.

driven testing, it is important to be able to define corresponding putative topographic ROIs in individual subjects *a priori*. In contrast, for exploratory analyses, one may wish to identify the likely topographical locus of some functional contrast (e.g., cluster or peak coordinate). In general, the MPM is useful for testing hypothesis-driven questions (Eickhoff et al. 2006), whereas the FPM is useful for exploratory analyses or interpreting patterns of functional activation (Eickhoff et al. 2007). Importantly, cross-validation procedures demonstrate that both the MPM (Fig. 11) and FPM (Fig. 10) are generally predictive of single-subject ROIs for novel subjects that did not contribute to the atlas generation.

The atlases provided here have many practical applications. First, the probabilistic atlas provides an unbiased approach to comparing the relative location of different functional activations with visual topography in meta-analyses. For example, we recently compared reported coordinates for grasping- and reaching-related activations from a series of fMRI studies in the parietal cortex (Konen et al. 2013). We compared these coordinates to the topographic regions of the IPS using our surface-based probabilistic atlas. In the spirit of the group-averaged metadata, this allowed an unbiased comparison that was not influenced by the topographic maps of any one subject. Importantly, the location of grasping- and reaching-related activity relative to the topographic regions as identified from the meta-analysis was consistent with data from individual subjects, where detailed topographic maps and functional activations were available for a direct comparison.

A second application of the probabilistic atlas is under conditions in which collecting the data to define maps in individual subjects is impractical or not feasible. For example, time-limitations and subject-fatigue both potentially limit the time researchers may be able to spend with patients suffering from neurological or neuropsychological disorders, or with implanted subdural or deep electrodes (e.g., ECoG). As an example, we have recently collected ECoG data from several epileptic patients who have a number of electrodes implanted on the surface of the parietal lobe (Wang et al. 2013). Although some of these electrodes are likely over visual topographic areas, it is impossible to assign these electrodes to a specific visual area without a functional benchmark. However, after aligning the individual subject

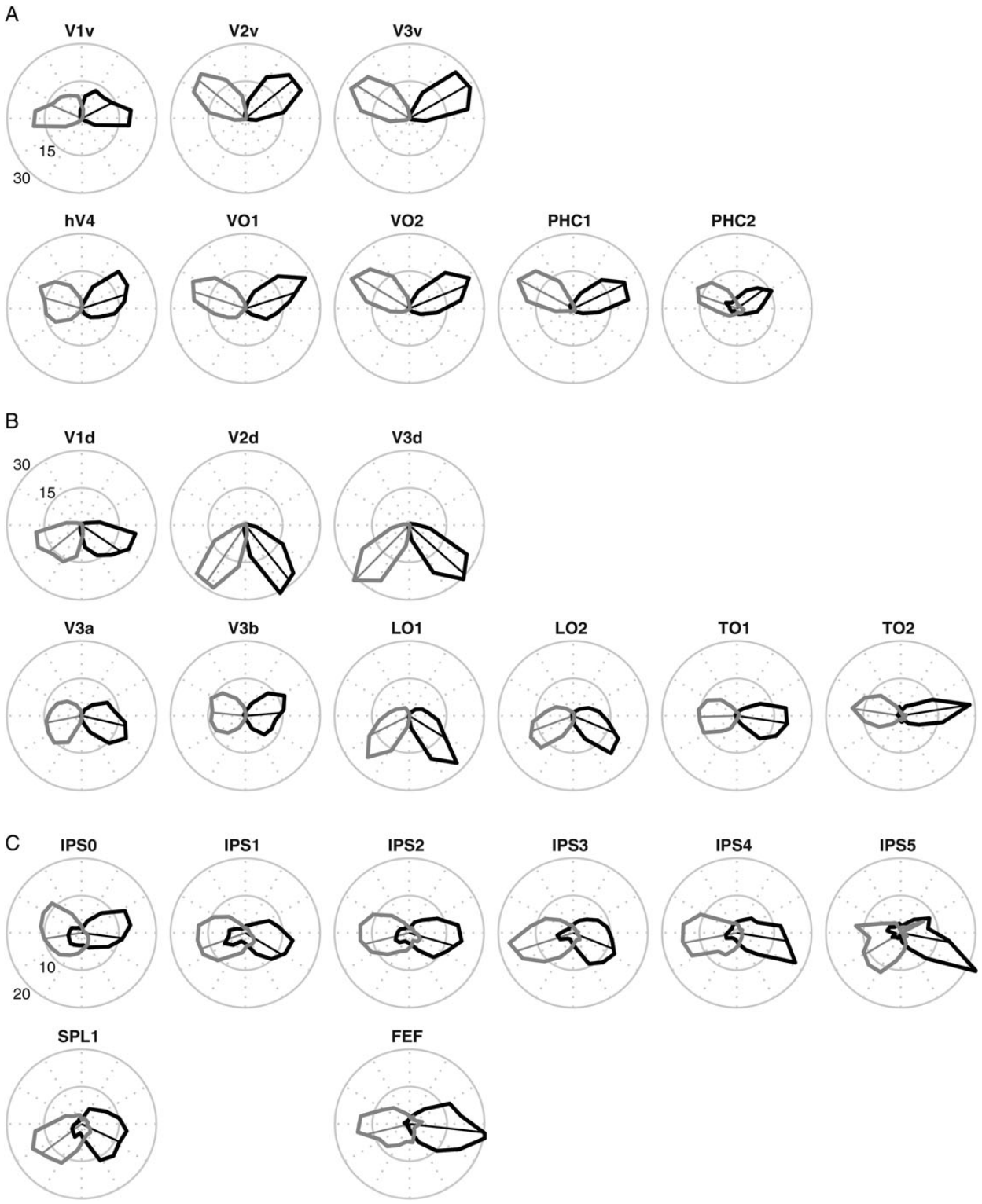

Figure 12. Visual field coverage for all ROIs in the SBA MPM. Polar angle histograms of the visual field coverage of the MPM projected onto novel subjects using the leave-one-out SBA. Polar angle phase values were extracted from data obtained using the retinotopy (*A* and *B*) or memory-guided saccade task (*C*) and concatenated across all subjects. Thick lines show the visual field coverage for the left (black) and right (gray) hemispheres as a proportion of the total coverage of an ROI. The thin-lined vectors represent the mean phase for a given ROI. As expected, all MPM ROIs projected to regions with a clear contralateral bias.

surfaces to our probabilistic atlas, we were able to identify some electrodes in visual areas, such as IPS2/3, and compare attention-related effects observed on these electrodes with the results from previous fMRI studies.

In a recent study, Abdollahi et al. (2014) generated a similar set of surface-based probabilistic area maps and MPMs for a set of 18 topographic areas across occipital– and lateral–temporal cortex. By comparing across 4 different inter-subject registration

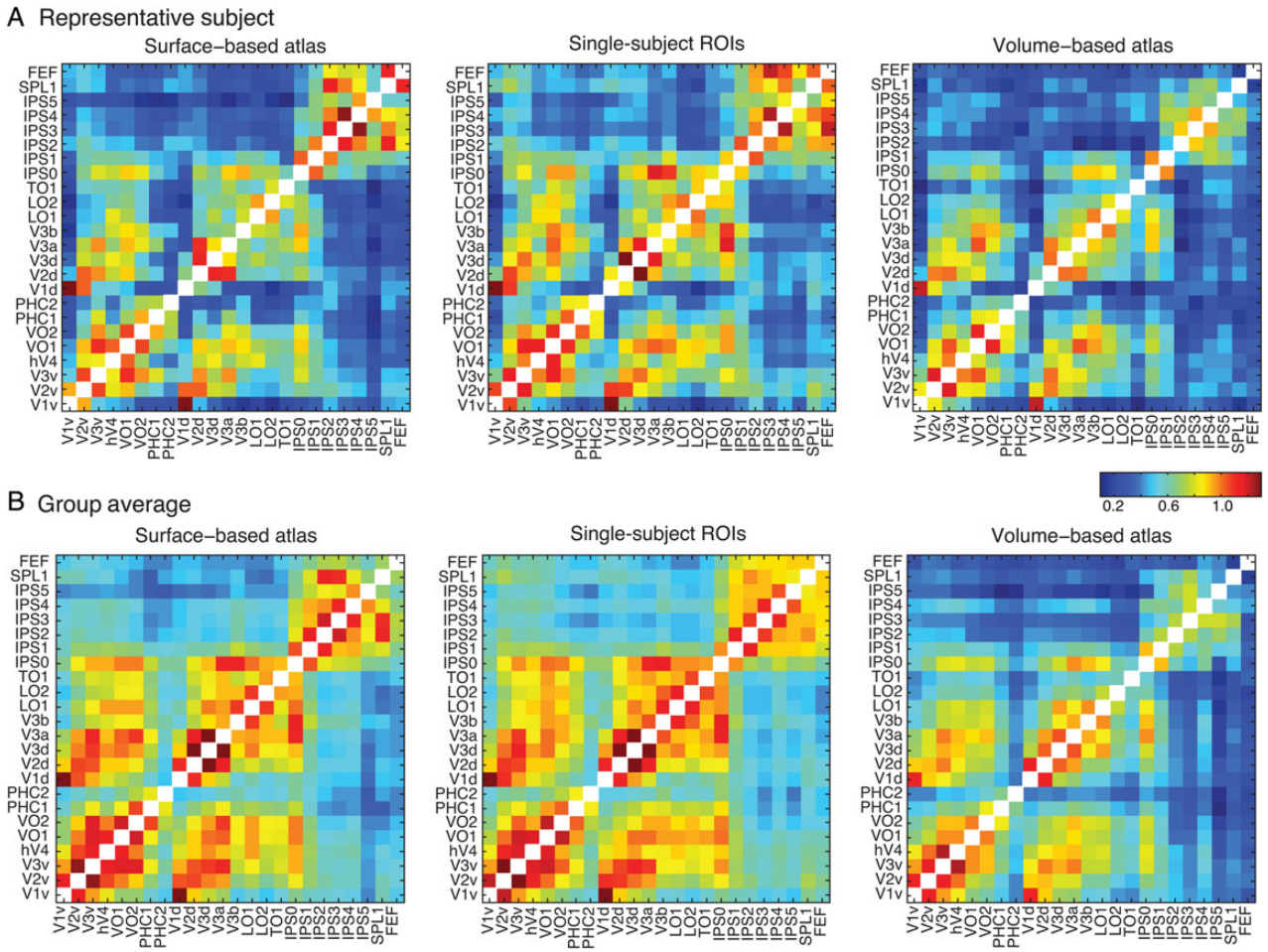

Figure 13. Resting-state functional connectivity across all ROIs in the probabilistic atlas. Values represent Fisher transformed correlations averaged across both hemispheres and 4 resting-state runs. (*A*) From a representative subject, functional connectivity matrix is calculated for surface-based atlas (left), subject-specific ROIs in the native volume space (center) and volume-based atlas with nonlinear transformation to the same native volume space (right). (*B*) The group-averaged functional connectivity is displayed using the same conventions. Notably, two panels of each column show similar distribution, which indicates strong connectivity within ventral–temporal, dorsal–lateral and parietal–frontal ROIs, as well as between two parts of ROIs, but weak connectivity between ventral–temporal (and dorsal–lateral) ROIs and parietal/frontal ROIs.

methods, they concluded that a multimodal surface matching method, which utilizes the retinotopic maps themselves for inter-subject alignment, produced the best set of MPMs. This study offers an important complement to the current dataset, although a few differences are worth noting. First, Abdollahi et al. (2014) derived their probabilistic atlas from a relatively small sample of 12 subjects, whereas our atlas is based on a much larger population, between 31 and 50 subjects depending on the ROI (Table 1). Second, our atlas and the one presented by Abdollahi et al. (2014) differ in the way in which certain regions of visual cortex were parcellated into distinct retinotopic regions. In particular, our studies used different criteria for defining ROIs in the region near our V3a/b and TO1/2. These differences are important given the current debate over the most appropriate way to define distinct functional regions in these areas of cortex (Orban et al. 2006; Georgieva et al. 2009; Silver and Kastner 2009; Kolster et al. 2010; Wandell and Winawer 2011). Finally, each study included topographic regions that are absent in the other atlas. Abdollahi et al. (2014) defined 2 topographic regions (phPITd and phPITv) in the region of cortex between hV4/VO1 and medial–temporal cortex. On the other hand, our study includes a comprehensive set of topographic maps in ventral–temporal (VO2 and PHC1-2), parietal (IPS1-5, SPL1), and frontal (hFEF) cortex. Overall, comparisons of these atlases in future studies may help shed light on the topographic divisions of human cortex.

In the current study, the majority of analyses that we performed revealed that the surface-based cortical normalization provided a superior alignment of visual topographic regions across subjects compared with the nonlinear MNI transformation in volume space. A variety of metrics including ROI size (Fig. 5), peak probability value (Fig. 6), central tendency (Fig. 7), and the blurring metric (Fig. 8) showed that the SBA displays more desirable properties compared to the VBA. The superiority of the SBA was also shown by the leave-one-out validation procedures. In particular, the MPM of the SBA showed better overlap with subject-specific ROIs in novel subjects than the VBA (Fig. 11). However, we did not observe a significant difference between the SBA and VBA in terms of the leave-one-out central tendency analysis quantifying the overlap between subject-specific ROIs and the FPM (Fig. 10). Thus, the largest advantages of the SBA were related to the use of the MPM, rather than the FPM. Overall, these comparisons suggest that the surface-based atlas would be preferred for future studies utilizing these atlases.

However, it is also important to keep in mind that the method used for registration to standard space (e.g., MNI or surface-space) will contribute to the inter-subject variability in anatomical alignment. Here, we used a cortical surface-based registration as implemented in FreeSurfer and SUMA or a nonlinear MNI transformation as implemented in FSL. Using alternate methods for spatial normalization or using the MNI-based atlas for surface-based data (after transforming the probabilistic atlas itself between normalized spaces) would necessarily result in additional variability that would not be captured by these atlases. Thus, it would seem most appropriate to use the surface-based atlas in the case where it is applied to data that have been transformed into the same standard space (i.e., Buckner40) using the same alignment method (i.e., FreeSurfer pipeline). However, Abdollahi et al. (2014) found that the atlas generated from their multimodal surface matching method provided the best match for novel subjects, even when the novel subject itself was aligned to the standard atlas space using an alternate (and presumably suboptimal) method. This suggests that the benefits of using the superior surface-based alignment for atlas generation may outweigh the additional variability introduced by aligning novel subjects to the standard atlas space using volume-based alignment algorithms.

In summary, we describe 2 probabilistic atlases of visual topographic regions of human cortex derived from a large population of subjects. Both the SBA and MNI VBA will be made freely available to the scientific community in formats that are compatible with several major neuroimaging analysis packages (see www.princeton.edu/~napl/vtpm.htm).

Supplementary Material

Supplementary material can be found at: http://www.cercor.oxfordjournals.org/.

Funding

This work was supported by the National Institutes of Health (RO1-MH64043, RO1-EY017699, and R21-EY021078 to S.K. and F32-NS063619 to R.E.B.M.), the National Science Foundation (BCS 1025149 to S.K.), the Natural Science Foundation of China (81371631 and 81422024 to L.W.) and Beijing Nova Program (Z141110001814068 to L.W.), Thousand Youth Talents Plan (Y4HX072006 to L.W.), and Hundred Talent Program of Chinese Academy of Sciences (Y3CX022003 to L.W.).

Notes

We would like to thank current and past members of the Kastner Lab, especially Stephanie McMains, Christina Konen, and Gideon Caplovitz, for help collecting and analyzing the mapping data. *Conflict of Interest*: None declared.

References

Abdollahi RO, Kolster H, Glasser MF, Robinson EC, Coalson TS, Dierker D, Jenkinson M, Van Essen DC, Orban GA. 2014. Correspondences between retinotopic areas and myelin maps in human visual cortex. NeuroImage. 99:509–524.

Amano K, Wandell BA, Dumoulin SO. 2009. Visual field maps, population receptive field sizes, and visual field coverage in the human MT+ complex. J Neurophysiol. 102:2704–2718.

Andersson JLR, Jenkinson M, Smith S. 2007. Non-linear registration, aka Spatial normalisation. FMRIB Analysis Group Technical Reports TR07JA2.

Arcaro MJ, McMains SA, Singer BD, Kastner S. 2009. Retinotopic organization of human ventral visual cortex. J Neurosci. 29:10638–10652.

Argall BD, Saad ZS, Beauchamp MS. 2006. Simplified intersubject averaging on the cortical surface using SUMA. Hum Brain Mapp. 27:14–27.

Bandettini PA, Jesmanowicz A, Wong EC, Hyde JS. 1993. Processing strategies for time-course data sets in functional MRI of the human brain. Magn Reson Med. 30:161–173.

Benson NC, Butt OH, Datta R, Radoeva PD, Brainard DH, Aguirre GK. 2012. The retinotopic organization of striate cortex is well predicted by surface topology. Curr Biol. 22:2081–2085.

Brainard DH. 1997. The psychophysics toolbox. Spat Vis. 10:433–436.

Bressler DW, Silver MA. 2010. Spatial attention improves reliability of fMRI retinotopic mapping signals in occipital and parietal cortex. NeuroImage. 53:526–533.

Brewer AA, Liu J, Wade AR, Wandell BA. 2005. Visual field maps and stimulus selectivity in human ventral occipital cortex. Nat Neurosci. 8:1102–1109.

Chen CH, Gutierrez ED, Thompson W, Panizzon MS, Jernigan TL, Eyler LT, Fennema-Notestine C, Jak AJ, Neale MC, Franz CE, et al. 2012. Hierarchical genetic organization of human cortical surface area. Science. 335:1634–1636.

Cohen AL, Fair DA, Dosenbach NU, Miezin FM, Dierker D, Van Essen DC, Schlaggar BL, Petersen SE. 2008. Defining functional areas in individual human brains using resting functional connectivity MRI. NeuroImage. 41:45–57.

Collins DL, Neelin P, Peters TM, Evans AC. 1994. Automatic 3D intersubject registration of MR volumetric data in standardized Talairach space. J Comput Assist Tomogr. 18:192–205.

Cox RW. 1996. AFNI: software for analysis and visualization of functional magnetic resonance neuroimages. Comput Biomed Res. 29:162–173.

Dale AM, Fischl B, Sereno MI. 1999. Cortical surface-based analysis. I. Segmentation and surface reconstruction. NeuroImage. 9:179–194.

DeYoe EA, Carman GJ, Bandettini P, Glickman S, Wieser J, Cox R, Miller D, Neitz J. 1996. Mapping striate and extrastriate visual areas in human cerebral cortex. Proc Natl Acad Sci USA. 93:2382–2386.

Dumoulin SO, Hoge RD, Baker CL Jr, Hess RF, Achtman RL, Evans AC. 2003. Automatic volumetric segmentation of human visual retinotopic cortex. NeuroImage. 18:576–587.

Eickhoff SB, Heim S, Zilles K, Amunts K. 2006. Testing anatomically specified hypotheses in functional imaging using cytoarchitectonic maps. NeuroImage. 32:570–582.

Eickhoff SB, Paus T, Caspers S, Grosbras MH, Evans AC, Zilles K, Amunts K. 2007. Assignment of functional activations to probabilistic cytoarchitectonic areas revisited. NeuroImage. 36:511–521.

Engel SA, Glover GH, Wandell BA. 1997. Retinotopic organization in human visual cortex and the spatial precision of functional MRI. Cereb Cortex. 7:181–192.

Felleman DJ, Van Essen DC. 1991. Distributed hierarchical processing in the primate cerebral cortex. Cereb Cortex. 1:1–47.

Fischl B, Sereno MI, Dale AM. 1999. Cortical surface-based analysis. II: Inflation, flattening, and a surface-based coordinate system. NeuroImage. 9:195–207.

Fischl B, Sereno MI, Tootell RB, Dale AM. 1999. High-resolution intersubject averaging and a coordinate system for the cortical surface. Hum Brain Mapp. 8:272–284.

Friston KJ, Frith CD, Liddle PF, Frackowiak RS. 1993. Functional connectivity: the principal-component analysis of large (PET) data sets. J Cereb Blood Flow Metab. 13:5–14.

Gattass R, Sousa AP, Gross CG. 1988. Visuotopic organization and extent of V3 and V4 of the macaque. J Neurosci. 8:1831–1845.

Georgieva S, Peeters R, Kolster H, Todd JT, Orban GA. 2009. The processing of three-dimensional shape from disparity in the human brain. J Neurosci. 29:727–742.

Hansen KA, Kay KN, Gallant JL. 2007. Topographic organization in and near human visual area V4. J Neurosci. 27:11896–11911.

Hinds OP, Rajendran N, Polimeni JR, Augustinack JC, Wiggins G, Wald LL, Diana Rosas H, Potthast A, Schwartz EL, Fischl B. 2008. Accurate prediction of V1 location from cortical folds in a surface coordinate system. NeuroImage. 39: 1585–1599.

Jenkinson M. 2001. Improved unwarping of EPI images using regularised B0 maps. NeuroImage. 13:S165.

Jezzard P, Balaban RS. 1995. Correction for geometric distortion in echo planar images from B0 field variations. Magn Reson Med. 34:65–73.

Kastner S, DeSimone K, Konen CS, Szczepanski SM, Weiner KS, Schneider KA. 2007. Topographic maps in human frontal cortex revealed in memory-guided saccade and spatial working-memory tasks. J Neurophysiol. 97:3494–3507.

Kolster H, Peeters R, Orban GA. 2010. The retinotopic organization of the human middle temporal area MT/V5 and its cortical neighbors. J Neurosci. 30:9801–9820.

Konen CS, Behrmann M, Nishimura M, Kastner S. 2011. The functional neuroanatomy of object agnosia: a case study. Neuron. 71:49–60.

Konen CS, Kastner S. 2008. Representation of eye movements and stimulus motion in topographically organized areas of human posterior parietal cortex. J Neurosci. 28:8361–8375.

Konen CS, Mruczek RE, Montoya JL, Kastner S. 2013. Functional organization of human posterior parietal cortex: grasping- and reaching-related activations relative to topographically organized cortex. J Neurophysiol. 109:2897–2908.

Larsson J, Heeger DJ. 2006. Two retinotopic visual areas in human lateral occipital cortex. J Neurosci. 26:13128–13142.

Meng X-L, Rosenthal R, Rubin DB. 1992. Comparing correlated correlation coefficients. Psychological Bulletin. 111:172.

Op de Beeck HP, Haushofer J, Kanwisher NG. 2008. Interpreting fMRI data: maps, modules and dimensions. Nat Rev Neurosci. 9:123–135.

Orban GA, Claeys K, Nelissen K, Smans R, Sunaert S, Todd JT, Wardak C, Durand JB, Vanduffel W. 2006. Mapping the parietal cortex of human and non-human primates. Neuropsychologia. 44:2647–2667.

Parvizi J, Jacques C, Foster BL, Witthoft N, Rangarajan V, Weiner KS, Grill-Spector K. 2012. Electrical stimulation of human fusiform face-selective regions distorts face perception. J Neurosci. 32:14915–14920.

Passingham RE, Stephan KE, Kotter R. 2002. The anatomical basis of functional localization in the cortex. Nat Rev Neurosci. 3:606–616.

Pelli DG. 1997. The VideoToolbox software for visual psychophysics: transforming numbers into movies. Spat Vis. 10:437–442.

Press WA, Brewer AA, Dougherty RF, Wade AR, Wandell BA. 2001. Visual areas and spatial summation in human visual cortex. Vision Res. 41:1321–1332.

Saad Z, Reynolds R, Cox RJ, Argall B, Japee S. 2004. SUMA: an interface for surface-based intra- and inter-subject analysis. Proc ISBI. 2:1510–1511.

Saxe R, Brett M, Kanwisher N. 2006. Divide and conquer: a defense of functional localizers. NeuroImage. 30:1088–1096. discussion 1097–1089.

Schleicher A, Palomero-Gallagher N, Morosan P, Eickhoff SB, Kowalski T, de Vos K, Amunts K, Zilles K. 2005. Quantitative architectural analysis: a new approach to cortical mapping. Anat Embryol (Berl). 210:373–386.

Schneider KA, Richter MC, Kastner S. 2004. Retinotopic organization and functional subdivisions of the human lateral geniculate nucleus: a high-resolution functional magnetic resonance imaging study. J Neurosci. 24:8975–8985.

Sereno MI, Dale AM, Reppas JB, Kwong KK, Belliveau JW, Brady TJ, Rosen BR, Tootell RB. 1995. Borders of multiple visual areas in humans revealed by functional magnetic resonance imaging. Science. 268:889–893.

Sereno MI, Pitzalis S, Martinez A. 2001. Mapping of contralateral space in retinotopic coordinates by a parietal cortical area in humans. Science. 294:1350–1354.

Silver MA, Kastner S. 2009. Topographic maps in human frontal and parietal cortex. Trends Cogn Sci. 13:488–495.

Smith AT, Greenlee MW, Singh KD, Kraemer FM, Hennig J. 1998. The processing of first- and second-order motion in human visual cortex assessed by functional magnetic resonance imaging (fMRI). J Neurosci. 18:3816–3830.

Smith SM, Jenkinson M, Woolrich MW, Beckmann CF, Behrens TE, Johansen-Berg H, Bannister PR, De Luca M, Drobnjak I, Flitney DE, et al. 2004. Advances in functional and structural MR image analysis and implementation as FSL. NeuroImage. 23(Suppl 1):S208–S219.

Smith SM, Miller KL, Salimi-Khorshidi G, Webster M, Beckmann CF, Nichols TE, Ramsey JD, Woolrich MW. 2011. Network modelling methods for FMRI. NeuroImage. 54:875–891.

Straw AD. 2008. Vision egg: an open-source library for realtime visual stimulus generation. Front Neuroinform. 2:4.

Swisher JD, Halko MA, Merabet LB, McMains SA, Somers DC. 2007. Visual topography of human intraparietal sulcus. J Neurosci. 27:5326–5337.

Tootell RB, Hadjikhani N, Hall EK, Marrett S, Vanduffel W, Vaughan JT, Dale AM. 1998. The retinotopy of visual spatial attention. Neuron. 21:1409–1422.

Tootell RB, Mendola JD, Hadjikhani NK, Ledden PJ, Liu AK, Reppas JB, Sereno MI, Dale AM. 1997. Functional analysis of V3A and related areas in human visual cortex. J Neurosci. 17:7060–7078.

Tzourio-Mazoyer N, Landeau B, Papathanassiou D, Crivello F, Etard O, Delcroix N, Mazoyer B, Joliot M. 2002. Automated anatomical labeling of activations in SPM using a macroscopic anatomical parcellation of the MNI MRI single-subject brain. NeuroImage. 15:273–289.

Wade AR, Brewer AA, Rieger JW, Wandell BA. 2002. Functional measurements of human ventral occipital cortex: retinotopy and colour. Philos Trans R Soc Lond B Biol Sci. 357:963–973.

Wandell BA, Dumoulin SO, Brewer AA. 2007. Visual field maps in human cortex. Neuron. 56:366–383.

Wandell BA, Winawer J. 2011. Imaging retinotopic maps in the human brain. Vision Res. 51:718–737.

Wang L, Saalmann YB, Shestyuk A, Crone NE, Parvizi J, Knight RT, Kastner S. 2013. Spike-phase coding of attention priorities in parietal cortex predicts behavior. Society for Neuroscience. 2013. San Diego. http://www.abstractsonline.com/plan/ViewAbstract.aspx?mID=3236&sKey=16feee7a-9366-4a71-95dc-cf18b05a7610&cKey=49ca2f87-ceea-4cb0-ae56-c50c26d73e96&mKey=8d2a5bec-4825-4cd6-9439-b42bb151d1cf.

Winawer J, Horiguchi H, Sayres RA, Amano K, Wandell BA. 2010. Mapping hV4 and ventral occipital cortex: the venous eclipse. J Vis. 10:1–22.

Witthoft N, Nguyen ML, Golarai G, Larocque KF, Liberman A, Smith ME, Grill-Spector K. 2013. Where is human V4? Predicting the location of hV4 and VO1 from cortical folding. Cereb Cortex. 24:2401–2408.

Woolrich MW, Jbabdi S, Patenaude B, Chappell M, Makni S, Behrens T, Beckmann C, Jenkinson M, Smith SM. 2009. Bayesian analysis of neuroimaging data in FSL. NeuroImage. 45:S173–S186.

Yeo BT, Krienen FM, Sepulcre J, Sabuncu MR, Lashkari D, Hollinshead M, Roffman JL, Smoller JW, Zollei L, Polimeni JR, et al. 2011. The organization of the human cerebral cortex estimated by intrinsic functional connectivity. J Neurophysiol. 106:1125–1165.

Zilles K, Amunts K. 2009. Receptor mapping: architecture of the human cerebral cortex. Curr Opin Neurol. 22:331–339.